Draft version November 21, 2023
Typeset using LaTeX twocolumn style in AASTeX631

THE NATURE OF X-RAYS FROM YOUNG STELLAR OBJECTS IN THE ORION NEBULA CLUSTER - A Chandra HETGS Legacy Project

Norbert S. Schulz,[1] David P. Huenemoerder,[1] David A. Principe,[1] Marc Gagne,[2] Hans Moritz Günther,[1] Joel Kastner,[3] Joy Nichols,[4] Andrew Pollock,[5] Thomas Preibisch,[6] Paola Testa,[4] Fabio Reale,[7] Fabio Favata,[8, 9] and Claude R. Canizares[1]

[1] *Department of Physics and Kavli Institute for Astrophysics and Space Research*
Massachusetts Institute of Technology
Cambridge, MA 02139, USA
[2] *West Chester University*
West Chester, PA 19383, USA
[3] *Center for Imaging Science, School of Physics & Astronomy, and Laboratory for Multiwavelength Astrophysics, Rochester Institute of Technology, 54 Lomb Memorial Drive, Rochester, NY 14623, USA*
[4] *Harvard & Smithsonian Center for Astrophysics*
Cambridge, MA 02138, USA
[5] *Department of Physics and Astronomy*
University of Sheffield Sheffield S10 2TN, United Kingdom
[6] *Universitäts-Sternwarte München, Ludwig-Maximilians-Universität,*
81679 München, Germany
[7] *University of Palermo*
90133 Palermo, Italy
[8] *ESA European Space Research and Technology Centre (ESTEC)*
Keplerlaan 1, 2201 AZ Noordwijk, The Netherlands
[9] *INAF - Osservatorio Astronomico di Palermo*
Piazza del Parlamento 1, 90134 Palermo, Italy

Abstract

The Orion Nebula Cluster (ONC) is the closest site of very young (~ 1 Myrs) massive star formation The ONC hosts more than 1600 young and X-ray bright stars with masses ranging from ~ 0.1 to 35 $M_\odot$. The *Chandra* HETGS Orion Legacy Project observed the ONC with the *Chandra* high energy transmission grating spectrometer (HETGS) for 2.2 Ms. We describe the spectral extraction and cleaning processes necessary to separate overlapping spectra. We obtained 36 high resolution spectra which includes a high brilliance X-ray spectrum of θ^1 Ori C with over 100 highly significant X-ray lines. The lines show Doppler broadening between 300 and 400 $\mathrm{km\,s^{-1}}$. Higher spectral diffraction orders allow us to resolve line components of high Z He-like triplets in θ^1 Ori C with unprecedented spectral resolution. Long term light curves spanning $\sim$20 years show all stars to be highly variable, including the massive stars. Spectral fitting with thermal coronal emission line models reveals that most sources show column densities of up to a few times $10^{22}\,\mathrm{cm^{-2}}$ and high coronal temperatures of 10 to 90 MK. We observe a bifurcation of the high temperature component where some stars show a high component of 40 MK, while others show above 60 MK indicating heavy flaring activity. Some lines are resolved with Doppler broadening above our threshold of $\sim 200\,\mathrm{km\,s^{-1}}$, up to $500\,\mathrm{km\,s^{-1}}$. This data set represents the largest collection of HETGS high resolution X-ray spectra from young pre-MS stars in a single star-forming region to date.

1. INTRODUCTION

The Orion Nebula Cluster (ONC) is a very young star forming region hosting a large number of young stellar objects in terms of mass, age, and evolutionary stages. The cluster is part of the Orion A molecular cloud hosting a hierarchical structure of ongoing star formation cells (Bally et al. 2000). The part of this region we generally refer to as the ONC is a somewhat older formation bubble located at the foreground of the main molecular cloud. Two very massive stars - θ^1 Ori C and θ^2 Ori A - are members of the Orion Trapezium Cluster at the core of the ONC with θ^1 Ori C being the main source of illumination and ionization of the Orion Nebula (M42).

The ONC also hosts a large assembly of young stars with about 80% of its members being younger than a few Myrs. With over 3000 stars in the vicinity of the Orion Trapezium the average stellar density amounts to about 250 stars per pc^3 within a radius of about 3 pc (Hillenbrand 1997). The ONC is the nearest site of massive star formation rich in a low- and intermediate mass pre-main sequence (PMS) stellar population as well as early-type zero-age main sequence (ZAMS) stars. It is well studied in the optical and infra-red bands with about 1600 sources classified to some limited extent through spectroscopic and photometric measurements (Hillenbrand 1997; Hillenbrand et al. 2013) and over 2000 stars being observed in the IR band with 2MASS (Skrutskie et al. 2006) and ground based surveys (Muench et al. 2002; Robberto et al. 2010; Manara et al. 2012).

The ONC also has a long history of X-ray observations. From its first discovery with *Uhuru* (Giacconi et al. 1972) identified as a bright X-ray source 3U0527-05 to the realization that this is a more extended emission region containing X-rays from stellar coronae around young T Tauri stars (den Boggende et al. 1978; Feigelson & Decampli 1981; Gagne et al. 1995), decades of observations established the ONC as one of the richest X-ray emitting star forming clusters. However, while most of these studies were severely limited by low angular resolution of their satellite telescopes, *ROSAT* in the 1990's came in best with 5 arcsec, a true breakthrough came with the launch of *Chandra* in 1999 which then offered an angular resolution of 0.5 to 2 arcseconds over a few arcmin field of view. The *Chandra* Orion Ultradeep Project (COUP, Feigelson et al. 2005) took full advantage of this superb observing capability and observed the ONC for nearly 10 days total to detect 1616 X-ray sources, measure column densities, source fluxes, and basic X-ray spectral and photometric parameters (Getman et al. 2005). Many X-ray surveys of other young stellar clusters were performed with *Chandra* , examples are RCW38 (Wolk et al. 2006), 30 Doradus (Townsley et al. 2006), NGC 6357 (Wang et al. 2007), M17 (Broos et al. 2007), NGC 2244 (Wang et al. 2008) or recently in the Tarantula Nebula (Crowther et al. 2022). Perhaps the most notable survey is the large Chandra Carina Complex Project, which detected over 14 000 X-ray sources, with a large number of multi-wavelength counterparts (Townsley et al. 2011; Broos et al. 2011; Gagné et al. 2011; Feigelson et al. 2011; Preibisch et al. 2011).

Young, low-mass (0.1 $M_\odot$ to about 2 $M_\odot$) pre-main sequence (PMS) stars are brighter in X-rays than their more evolved counterparts on the main sequence. The ratio of X-ray to bolometric luminosity in these stars lies between 10^{-4} and 10^{-3}, close to the saturation threshold (Vilhu 1984; Vilhu & Walter 1987; Wright et al. 2011). Besides coronal activity, accretion and outflows can also contribute X-ray flux for those stars still surrounded by a proto-planetary disk (for a review, see Schneider et al. 2022). Those stars are called classical T Tauri stars (CTTS). X-rays from shocks in outflows are very soft and orders of magnitude fainter than coronal emission (Güdel et al. 2011); they can generally only be seen in near-by stars with little absorption where the jet is spatially resolved. One of the first detections of soft X-rays from shocks at the base of an outflow was an Orion proplyd using the COUP dataset (Kastner et al. 2005). Another source of X-rays is the accretion shock itself. The disk does not reach down to the star, but instead mass falls onto the stellar surface along the magnetic field lines. It is accelerated to free-fall velocities and forms a strong shock at the stellar surface. This shock heats the infalling gas to X-ray emitting temperatures (Lamzin 1998; Günther et al. 2007; Hartmann et al. 2016). The density in the shock is high enough that it alters the line ratios in the He-like triplets, which are resolved in high-resolution X-ray grating spectroscopy (e.g. Kastner et al. 2002, 2004; Testa et al. 2004; Schmitt et al. 2005; Günther et al. 2006; Argiroffi et al. 2007; Brickhouse et al. 2010; Argiroffi et al. 2012). However, it is not clear if it is actually the shock itself that is observed (Reale et al. 2013, 2014), or if the depth of the shock in the photosphere and the outer layers of an inhomogenous accretion column hide the shock from view (Sacco et al. 2010; Schneider et al. 2018; Espaillat et al. 2021), and the observed line-ratios would be a secondary effect, formed where cooler and denser plasma flows up into the corona as seen in simulations (Orlando et al. 2010, 2013).

Older weak-lined T Tauri stars (WTTS) do not show accretion and thus have coronal line ratios in their He-like triplets, e.g., in the WTTS HID 98890 (e.g., Kastner et al. 2004). Telleschi et al. (2007) also showed that many CTTS have hard spectra with substantial emissions up to 10 keV, far beyond the reach of accretion shock heated plasma. Yet, in the accretion phase the stars accrete not only mass, but also angular momentum; young stars, CTTS and WTTS, thus rotate faster than their older main-sequence counterparts, which explains the saturated level of coronal activity. This fact is often used to identify young stars in a dense field, e.g., Pillitteri et al. (2013) use X-ray observations in the Orion A cloud south of the ONC to find young, but disk-less cluster members.

Performing high spectral resolution X-ray studies of very young stellar clusters is challenging. The *Chandra* High Energy Resolution Transmission Grating Spectrometer (HETGS) disperses the image of a point source across the field of view (see Canizares et al. 2000). This works well for isolated objects, but is susceptible to confusion from intersecting and overlapping spectra in crowded fields, such as young stellar associations. HETGS spectra of the close by TW Hydra association were easy to obtain because the member stars are sufficiently well separated in individual pointings (Kastner et al. 2002, 2004; Huenemoerder et al. 2007). Stars of the Cygnus OB2 association fit into one single pointing, but they are still sufficiently well separated to prevent serious confusion (Waldron et al. 2004).

The ONC is the nearest massive star forming cluster at a distance of $\simeq 400$ pc (Menten et al. 2007; Kounkel et al. 2017; Kuhn et al. 2019; Maíz Apellániz et al. 2022). Its brightest sources were a focus early in the *Chandra* mission, involving θ^1 Ori A, C and E (Schulz et al. 2003; Gagné et al. 2005; Huenemoerder et al. 2009), and θ^2 Ori A (Schulz et al. 2006; Mitschang et al. 2011). Schulz et al. (2015) used an early set of *Chandra* HETG observations to study 6 bright PMS stars in the near environment of the Orion Trapezium at the core of the ONC. Here significant confusion between overlapping spectra was encountered. That study specified the limitations of high angular resolution as offered by the *Chandra* optics and dispersive high resolution spectroscopy offered by the HETGS. In the ONC field of view the closest separation within bright sources is between 5 to 8 arcsec which appeared to make a deep high resolution study feasible. However, it also indicated that even though the angular resolution of *Chandra* is 0.5 arcsec, dispersive studies of PMS stars separated by less then 3-5 arcsec are not feasible. The study by Huenemoerder et al. (2007) of Hen 3-600 shows this limitation well for a 1.5 arscec binary. This excludes all clusters more distant than the ONC.

In this paper we describe our observation of the ONC with the *Chandra* HETGS in order to obtain more than 3 dozen high resolution X-ray grating spectra of ONC member stars. We present observations, spectral confusion cleaning procedures, a set of final spectra bearing a total number of counts and exposure time after spectral cleaning and a first in depth analysis of X-ray properties of massive, intermediate mass stars and low-mass PMS stars in the ONC for which we have sufficient spectral data.

2. OBSERVATIONS AND DATA REDUCTION

2.1. *The Chandra HETGS*

The *Chandra* HETG assembly consists of an array of periodic gold microstructures that can be interposed in the converging X-ray beam just behind the *Chandra* High Resolution Mirror Assembly. When the telescope observes a point source with the gratings in place, a fraction of the X-rays are dispersed, according to wavelength, to either side of the point source zeroth-order image. The zeroth order image and the dispersed +/- first and less prominent higher orders are detected at the focal plane by the linear array of CCD detectors, ACIS-S. Thus the whole system of mirror, gratings and detector constitute a slitless spectrometer, the HETGS (Canizares et al. 2000). The HETG assembly has two different grating types, designated MEG and HEG, optimized for medium and high energies, respectively. The gratings are mounted so that the dispersed +/- spectra of the MEG and HEG are offset from one another by an angle of 10 degrees, forming a shallow "X" in the focal plane with the zeroth order image at its center (Fig. 2).

The HETGS provides spectral resolving powers of $\lambda/\Delta\lambda = 100 - 1000$ in its first orders for point sources, corresponding to a line FWHM of about 0.02Å for MEG and 0.01Å for HEG, and effective areas of 1-180 cm^2 over the wavelength range of 1.2-30Å (0.4-10 keV). Multiple overlapping orders are separated using the moderate-energy resolution of ACIS-S.

2.2. *HETGS Observations*

The data contains a set of 70 observations of the ONC with the HETG aimed at the central star of the Orion Trapezium θ^1 Ori C. The total amount of the exposure is 2,086.14 ks taken over a period of about 20 years. The top right inset of Fig 1 shows the merged image of all observations over the most effective field of view summed over all roll angles. Nearly all visible dispersive HETG streaks are due the three brightest sources in the field, θ^1 Ori C, θ^1 Ori E, and MT Ori. The observations are divided into two suites; one taken over six years after the launch of *Chandra* in 1999 amounting to 470.96 ks summarized in Tab.1 and a second suite during the years 2019 and 2020 amounting to a total of 1615.18 ks. The latter suite is separated into two periods before (Tab.2) and after sun block (Tab.3) of the Orion region.

The first suite of data were all taken during a time period of 1999 and 2007 and were performed using the full array of ACIS-S CCD devices. This means for these data full access of the *Chandra* wavelength band is available from 1.70 Å to 30 Å. These observations also provide the bulk of X-rays above 16 Ådue to progressing ACIS contamination at later stages in the *Chandra* mission.

The second suite of observations was taken about 13 years later, after the observing conditions of the satellite had changed. Progressing contamination of the focal plane CCD array optical blocking filter effectively blocks

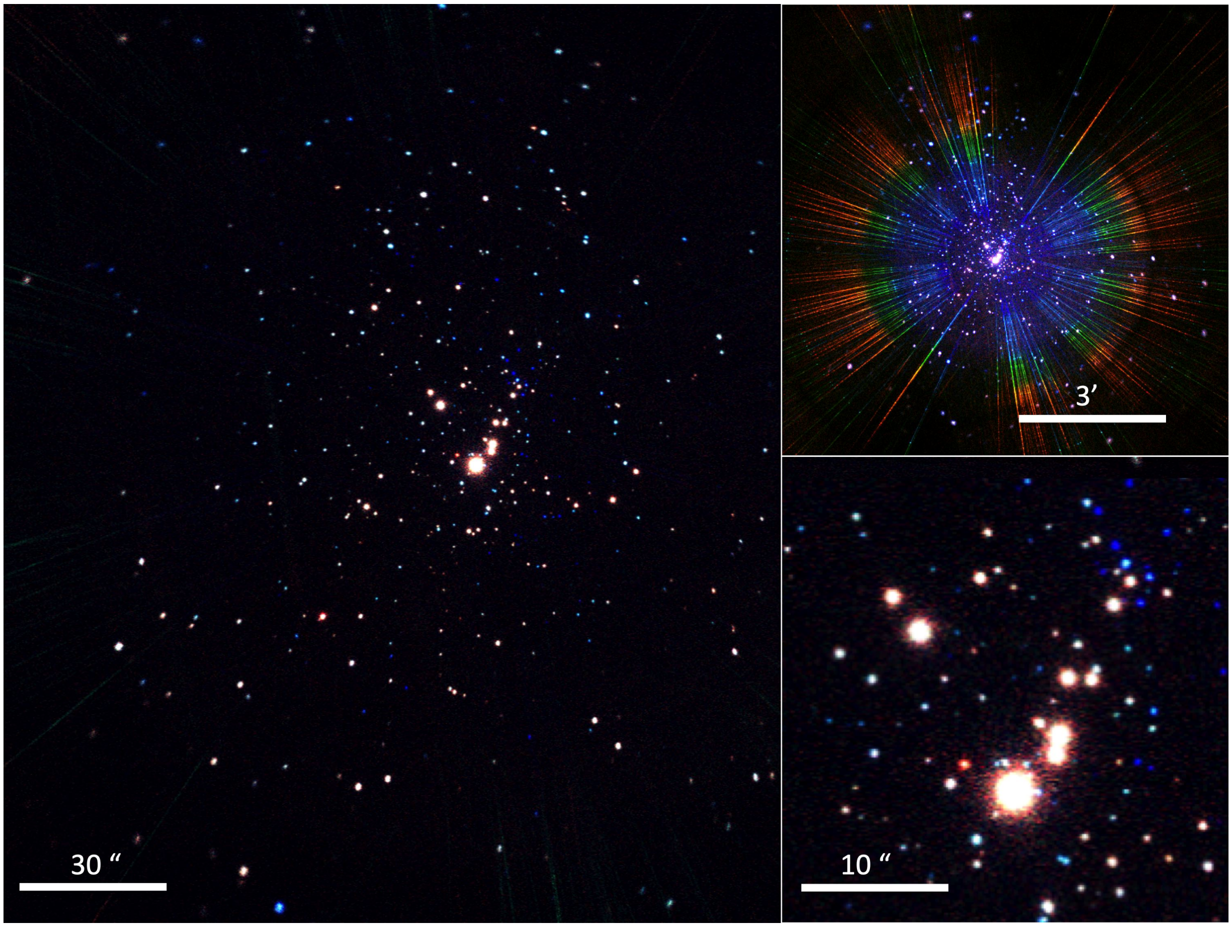

Figure 1. Merged zero order image over the entire exposure using a three color (rgb) scheme reflecting the stars energy spectra. The main image is shown with a 30 arcsec scale covering about 60% of the entire captured ACIS-S field of view. The dispersive HETG 1st and higher order dispersion events of the brightest star θ^1 Ori C were removed. The top right inset shows a wider view for 3 armin with all dispersion streaks included. The most prominent one are from θ^1 Ori C. The bottom right inset shows a zoomed version of the Orion Trapezium region, which includes about 10 of the brightest stars in the region and for which we have most significant HETG 1st order spectra.

soft X-rays below 1 keV (> 12.3485 Å). In addition, thermal constraints due to deteriorating thermal protection of the spacecraft requires reducing the number of CCD devices activated during observations. We added a column in Tab. 2 and Tab. 3 listing the number of CCD devices active during the observation. For 6 CCDs we have the full wavelength band available; for 5 CCDs this still holds, but we lose some exposure above about 24 Å; for 4 CCDs we lose exposure above about 18 Å. This is not an additional limitation, however, as the progressive ACIS filter contamination blocks most of the exposure above 16 Å anyway.

2.3. *Spectral Extraction*

For most data preparation and spectral analysis we used the Interactive Spectral Interpretation System (ISIS) (Houck & Denicola 2000). To uniformly process the many observations each with multiple objects of interest in a crowded field, we modified the standard procedures of the CIAO software (Fruscione et al. 2006). Events were rerun through standard event processing to update bad pixel maps and to "destreak" bad events on CCD_ID 8 (ACIS-S4). We then reran *acis_process_events* to re-create a Level 1 event file identical to what is done in standard processing. Since we have many observations with an ensemble of sources of interest in a crowded field, we matched and updated the world-coordinate-system (WCS). This is so that we can run source spectral extractions using *a priori* source celestial coordinates from COUP (Getman et al. 2005). This avoids small position uncertainties in zeroth order detection due to low exposure or confusion by dispersed spectra. We then simply skip the detection step and map the celestial coordinates to sky pixel for each observation using the WCS. In order to provide the WCS registration, we ran a CIAO source detection program,

Table 1. CHANDRA HETGS Observations before 2008

Obsid	Exp. [ks]	Date [UT]	Time [UT]	MJD [d]
3	49.62	1999-10-31	05:47:21	51482.2
4	30.92	1999-11-24	05:37:54	51506.2
2567	46.36	2001-12-28	12:25:56	52271.5
2568	46.34	2002-01-19	20:29:42	52324.9
7407	24.64	2006-12-03	19:07:48	54072.8
7408	24.98	2006-12-19	14:17:30	54075.5
7409	27.09	2006-12-23	00:47:40	54088.6
7410	13.10	2006-12-06	12:11:37	54092.0
7411	24.64	2007-07-27	20:41;22	54308.9
7412	25.20	2007-07-28	06:16:09	54309.3
8568	36.08	2007-08-06	06:54:08	54318.3
8589	50.71	2007-08-08	21:30:35	54320.9
8895	24.97	2007-12-07	03:14:07	54419.4
8896	22.66	2007-11-30	21:58:31	54434.8
8897	23.65	2007-11-15	10:03:16	54441.1

Table 2. CHANDRA HETGS Observations from 2019/20 before sun block

Obsid	Exp. [ks]	Date [UT]	Time [UT]	CCD	MJD [d]
23008	47.43	2019-11-27	12:07:33	4	58814.5
22893	24.73	2019-12-02	17:18:23	5	58819.7
22994	24.73	2019-12-05	09:22:57	4	58822.4
23087	39.54	2019-12-08	16:56:56	4	58825.7
22904	36.58	2019-12-10	17:49:59	4	58827.7
23097	35.88	2019-12-11	12:12:24	4	58828.5
22337	37.66	2019-12-13	04:25:33	4	58830.2
23006	24.73	2019-12-14	06:35:20	5	58831.3
22343	24.73	2019-12-15	20:04:15	4	58832.8
23003	24.74	2019-12-21	05:12:39	4	58838.2
23104	24.73	2019-12-21	21:47:04	5	58838.9
22336	25.59	2019-12-22	11:01:50	4	58839.5
23007	37.41	2019-12-24	23:12:06	4	58842.0
22339	31.64	2019-12-26	02:06:17	4	58843,1
22892	30.66	2019-12-26	22:46:53	4	58843.9
22995	38.74	2019-12-27	14:29:16	4	58844.6
22338	39.15	2019-12-30	06:02:12	4	58847.3
22334	24.73	2019-12-31	09:17:51	4	58849.3
23000	42.50	2020-01-01	07:04:24	4	58851.7
22996	26.70	2020-01-03	00:38:17	5	58852.4
23114	37.56	2020-01-03	16:46:28	4	58855.0
23115	29.67	2020-01-04	10:02:01	4	58856.5
22335	29.67	2020-01-06	23:19:34	4	58859.55
23005	24.73	2020-01-08	10:14:19	5	58941.05
23120	39.54	2020-01-11	12:12:26	4	58941.6
23012	10.81	2020-04-01	23:58:25	6	58943.86
23206	17.71	2020-04-02	13:57:51	6	58944.4
23207	14.75	2020-04-04	12:21:33	6	58948.4
23208	14.75	2020-04-05	08:54:30	6	58951.0
23011	51.69	2020-04-21	18:33:18	5	58960.8
22341	32.12	2020-04-29	09:07:29	5	58968.4
23233	34.59	2020-05-01	13:36:01	5	58970.6
23010	25.72	2020-07-27	11:07:30	4	59057.5
23001	25.62	2020-07-28	05:42:17	6	59058.2
23009	25.01	2020-07-28	23:57:16	6	59059.0

wavdetect, on the central region over an 8 arcmin radius for several spatial scales. For that we used a PSF-map which we created using *mkpsfmap* at 2.3 keV for an enclosed counts fraction of 0.9. We then applied *wcs_match* to fit the rotation and translation of the coordinate system of each ObsID relative to COUP, and updated all Level 1 event files and corresponding aspect solution files with these solutions. Spectral extraction then followed the usual CIAO steps but with narrower than default cross-dispersion extraction regions to reduce the overlap of crossing HEG or MEG orders from different sources. This does not change the overall spectral extraction process, but reduces the ambiguity about from which source an event originates in the extraction mask.

Responses were made in the usual way for each source extraction, via the CIAO commands *mkgrmf* and *mkgarf*. While ARFs depend critically on source position and observation details (such as the aspect history), RMFs do not. The RMFs depend on the spectral extraction region width which we chose to be the same for all sources and observations. Thus, there are only four unique RMFs for HEG and MEG ±1 orders for all sources.

2.4. *Confusion Analysis*

The region of the sky observed by the HETGS includes more than 1000 known X-ray sources (Fig 1) and the majority of these are present in the field of view of individual epochs. The HETGS instrument disperses light from each X-ray source in a characteristic, shallow

Table 3. CHANDRA HETGS Observations from 2019/20 after sun block

Obsid	Exp. [ks]	Date [UT]	Time [UT]	CCD	MJD [d
22340	25.62	2020-10-14	17:14:19	6	59136.7
24832	27.59	2020-10-15	05:57:17	6	59137.3
22997	26.60	2020-10-15	18:40:16	6	59137.8
24834	26.91	2020-10-16	07:35:44	5	59138.3
22342	34.50	2020-10-20	03:07:56	6	59142.1
24842	29.57	2020-10-21	01:56:20	6	59143.1
22993	24.63	2020-10-23	05:55:39	6	59145.3
22998	23.09	2020-11-01	04:40:26	5	59154.2
22999	35.58	2020-11-08	07:34:20	5	59161.3
24830	26.52	2020-11-22	07:56:09	4	59175.3
24622	24.56	2020-11-23	09:17:18	4	59176.4
24873	24.74	2020-11-24	03:01:16	4	59177.1
24874	25.72	2020-11-24	15:24:52	4	59177.6
24829	26.46	2020-11-27	14:58:09	4	59180.6
24623	24.74	2020-11-29	13:30:17	4	59182.6
24624	29.67	2020-12-09	22:23:51	4	59192.9
23002	30.66	2020-12-10	13:20:39	4	59193.6
23004	32.14	2020-12-12	01:34:32	4	59195.1
24831	30.66	2020-12-25	05:12:20	4	59208.2
24906	28.60	2020-12-25	21:09:10	4	59208.9

'X' shape on the ACIS-S detectors[1]. The non-dispersed (0th order) events are located at the right ascension (RA) and declination (DEC) of the X-ray source in the sky. The first, second and third order events for each source are dispersed by an angle given by the dispersion equation. The orders overlap along a line, one pair for the +/- HEG and one for the +/- MEG. While every X-ray source in an HETGS field of view has its light dispersed in the characteristic X-shaped pattern, only those sources that are sufficiently bright will disperse enough events to yield meaningful spectra.

HETGS observations of crowded fields, where multiple bright point sources cast their X-shaped patterns on the CCDs, suffer from event confusion, a scenario where events from two (or more) astrophysical sources could arrive at the same location on the detector and be erroneously assigned with standard CIAO processing (Fig. 2, Top). The relative locations of the dispersed spectra for each source depend on the roll angle of the observation. Dispersed spectra roll with the spacecraft, but zeroth order sky positions do not. Hence, the relative positions of spectra change with roll and every epoch in the ONC HETGS dataset will have unique sources of confusion (Fig 1). To identify and account for all the potential sources of confusion when extracting spectra, we created a custom Python program called *CrissCross* which utilizes the fixed geometry of the X-shaped spectral dispersion region and the known location of X-ray sources in the field of view to produce un-confused spectra. While the details of *CrissCross* will be published in a forthcoming paper (Principe et al. in prep), we summarize its utility here.

In the ONC HETGS dataset, there are three primary causes of confusion when assigning events to a specific source for spectral extraction: (a) 0th order (non-dispersed) point sources falling on a extracted sources spectral arm, (b) dispersed events from one source intersecting the arm of an extracted source, and (c) a bright source whose 0th order lands on or near another sources spectral arm dispersing its events along the same location on the CCD (Fig. 2, left). The location where confusion occurs in the spectrum of an extracted source is straightforward to calculate using the location on the CCD of the confuser and the well-calibrated energy to dispersion distance relation for HEG and MEG.

Standard CIAO processing already mitigates some portion of confusion by utilizing ACIS order sorting (Fig. 2, right). When events are assigned to a specific source during spectral extraction, the CCD-resolved event energy is compared to the expected energy of the event based on its dispersion distance (i.e., the distance from the 0th order in the dispersion direction). If these energies do not match, within an energy range based on the spectral energy resolution of the CCD, then events from a confusing source will automatically be rejected from the extracted spectrum, effectively removing confusion. However, in a region with a large number of X-ray sources like the ONC, there are often cases where the CCD-resolved energy of confusing events happens to match the expected energy of dispersed events during spectral extraction. In these cases ACIS order sorting will erroneously assign events from a confusing source to the extracted spectrum. Therefore, we use *CrissCross* to identify scenarios where this confusion occurs so that we can account for this during spectral fitting.

CrissCross is run for each observation and ultimately identifies all three sources of confusion for every source of interest (e.g., Table 4). In order to achieve this goal *CrissCross* runs through multiple steps starting with building a source list of all detected point sources and

[1] https://cxc.harvard.edu/proposer/POG/

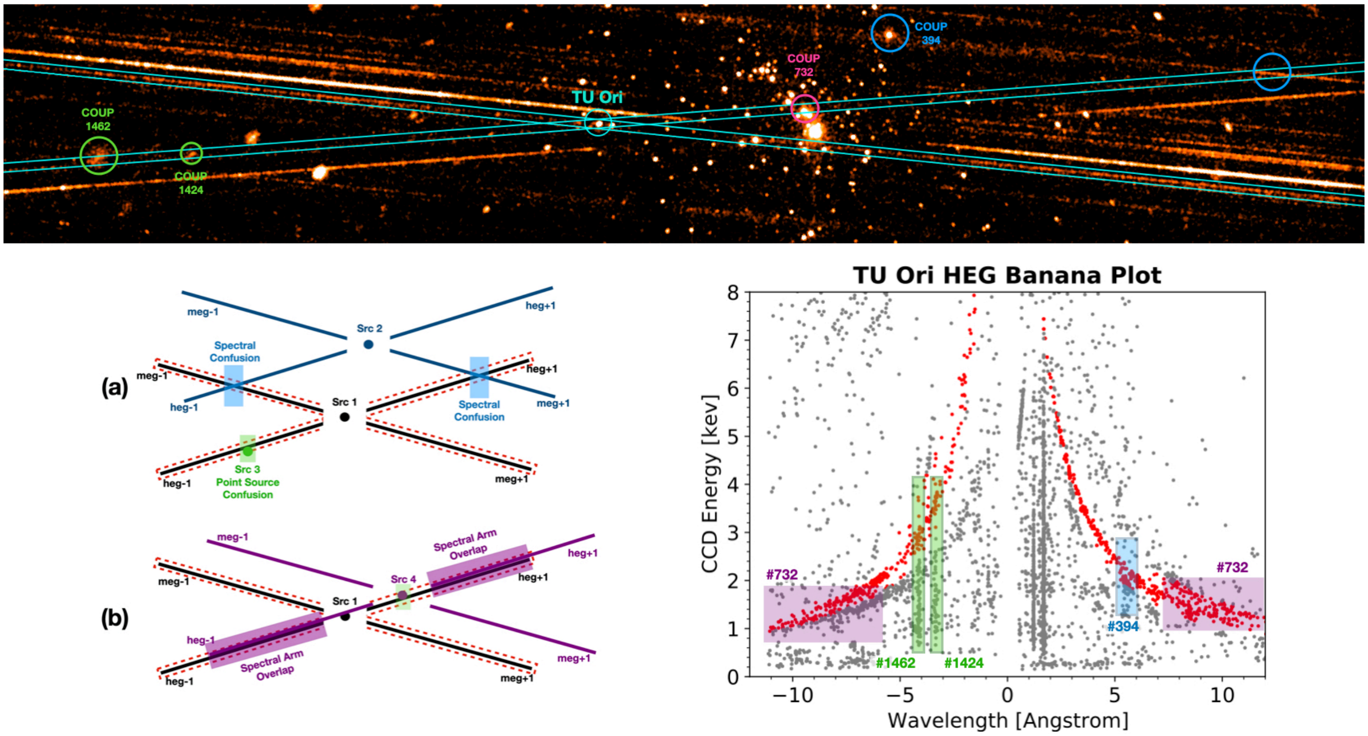

Figure 2. Top: An example HETG observation (obsid 3) demonstrating the need to account for confusion when extracting spectra in the ONC dataset. An example dispersed spectrum of TU Ori is displayed (cyan rectangle) with sources of confusion highlighted with circles (green-point source confusion, blue- spectral confusion, magenta-spectral arm overlap). Left: An illustration (not to scale) demonstrating (a) point source (green) and spectral (blue) confusion and (b) spectral arm confusion (magenta). The black X labeled Src 1 corresponds to the source intended for spectral extraction with the red dashed box corresponding to dispersed events. Specific locations in the extracted spectra where confusion can occur are identified with colored boxes. Right: ACIS order sorting banana plot showing confused events from different sources in the field erroneously being assigned to the spectra of TU Ori. Red dots indicate events that standard CIAO processing assigns to the extracted source (TU Ori) while other events, whose ccd-resolved energy do not match the expected wavelength of TU Ori, are not included in the standard CIAO source extraction. Colored numbers represent the COUP number of the source causing confusion for this case. Examples where standard CIAO processing has the potential to erroneously include events from other sources in the extracted spectrum of TU Ori are shown as red dots within the colored boxes.

an estimation of their brightness in terms of counts per observation. This is achieved with *wavdetect* which identifies sources with a Mexican-Hat Wavelet source detection algorithm. However, *wavdetect* is not designed to be run on grating observations where HETG dispersed events are often misidentified as point sources. Nevertheless, the *wavdetect* tool still correctly identifies point sources and we cross match all *wavdetect* sources to the list of known COUP sources (Feigelson et al. 2005). If a detected source is within 3 arcseconds of a COUP source then it is recognized as a valid source. If more than one *wavdetect* source is detected within 3 arcseconds of a known COUP source, the closest source is assigned to the COUP source. The majority of cluster members are near the center of the field of view where 0th order events dominate (Fig 1) and thus their detection is not affected by dispersed events. Off-axis COUP point sources were also accurately matched. The location of 0th order point sources and the estimated number of counts for each source provided by *wavdetect* is used to calculate the location of every dispersed spectrum in each field of view. All three primary causes of confusion are then identified for every source in Table 4. The ONC HETGS observations were carried out with ACIS-S while the COUP project used ACIS-I. Since the ACIS-S array covers a larger area of the sky, there are 27 X-ray sources detected in the HETGS ONC observations that were outside of the field of view of the COUP. Regardless of whether or not these sources represent young stars in the ONC, we include these objects when considering spectral confusion of the bright HETGS sources. All of these X-ray sources have 2MASS counterparts.

Point source confusion occurs when a 0th order point source is detected on or near an HEG or MEG arm of an extracted source within some margin. Since the Chandra PSF increases in radius as a function of distance off-axis (i.e., distance from the optical axis, or aimpoint), the margin used to initially determine whether a point source is a confuser also depends on off-axis angle. A point source located within 3 arcminutes of the aimpoint is initially considered a potential confusing source if its centroid is located within 8 pixels (∼4 arcsec) of the dispersed arm in the cross dispersion direction (perpendicular to the arm on the CCD). If a source is considered confusing, the energy and number of events within the fraction of the PSF that overlaps with the spectral arm of the extracted source is estimated. The number of 0th order counts in the same energy range for the source intended for spectral extraction is also determined. If the confusing source contributes more than 10% of the counts in the specific energy range where confusion occurs then it is considered a genuine case of point source confusion.

Spectral confusion occurs when the dispersed spectrum of a confusing source intersects with the dispersed spectrum of the source intended for spectral extraction. In most cases, this type of event confusion is already removed with ACIS order sorting under standard CIAO processing. However, if the location where the two spectra intersect corresponds to the same energy in both spectra (i.e., the confusing events are within the order sorting energy range of the extracted spectrum) then genuine confusion will occur and the confusing events could be erroneously assigned to the extracted source's spectrum. *CrissCross* identifies these cases and determines the number of counts in both the confuser and extracted sources 0th orders in the same energy range. After accounting for the different efficiencies between HEG and MEG spectral arms, if the ratio of 0th order confuser counts to 0th order extracted counts is greater than 15% it is considered a genuine source of spectral confusion.

The final primary cause of confusion in the ONC HETGS dataset comes from spectral arm confusion. Cases of spectral arm confusion occur when a bright 0th order point source (e.g., a source bright enough to disperse many events in the 1st order) falls on or near the spectral arm of a source intended for extraction. Identifying potential cases of spectral arm confusion begins by identifying 0th order point sources with more than 50 counts that fall within a specific cross-dispersion distance of the intended source for spectral extraction. As is the case with point source confusion, we consider off-axis angle when determining an appropriate cross dispersion distance for potential confusion. A single on-axis source will have a cross-dispersion width of about ∼4 arcsec (8 pixels). As the PSF gets larger farther off-axis, the cross-dispersion distance used to identify confusing sources is increased based on the off-axis locations of both the confusing and the intended source for spectral extraction.

Unlike other sources of confusion, spectral arm confusion has the potential to contaminate the entire HEG or MEG arm of the source intended for extraction. If the 0th order location of the two sources are close enough in the dispersion direction, many of the confusing spectral events can fall in an energy window that the extracted source is expecting (i.e., ACIS order sorting would erroneously assign events from the confused source to the extracted source). For every potential arm confusing case, *CrissCross* uses the distance between two 0th orders in the dispersion direction to evaluate the boundaries in energy space within a spectrum where a standard spectral extraction would have erroneously included events from the confused source. These spectral regions are then flagged as confused and accounted for in spectral fitting (Section 2.5).

The three causes of confusion were determined for every source in Table 4 on a per-epoch basis and collated into a master table to be used in spectral cleaning (Section 2.5). The reduction and analysis of the high resolution X-ray spectra in Tab.4 from the 70 HETGS observations of the ONC represents a very large dataset with tens of thousands of potential instances of confusion over all the individual spectra. Many instances of confusion were checked by eye but it is not feasible to check them all. Therefore, conservative parameter values were chosen with *CrissCross* to err on the side of removing some genuine source events in an effort to ensure confusion events are not included in our final spectral extractions. This provides a first set of quality spectra for analysis.

2.5. *Spectral Cleaning Process*

The spectral extraction results in standard products for data analysis for all sources over the entire exposure. This includes a PHA file containing binned spectra, and their corresponding ARFs and RMFs. We did not extract backgrounds adjacent to spectra, since the "background" will be largely due to confusing sources, both zeroth orders and dispersed spectra as described in Sec.2.4. For this analysis we combine the single source spectra (i.e. PHA files) to one merged spectrum but ignore the confused regions. To do this, we load all the spectra for a given source, then apply the confusion information which defines the regions to be ignored in each order of each spectrum. The confusion analysis described in Sec. 2.4 produced a confusion table which contains all locations where cluster stars interfere with each other either via zero order overlaps with grating arms spatially or where grating arms overlap with each other spatially *and* in PHA space. In standard analysis of a single, isolated source, the PHA is used to sort the grating orders. In a multi-source confused situation as we encounter in the ONC, PHA space also has to sort out orders from other confusing sources. The application of the information from the confusion table is straightforward for the zero order point source overlaps, but somewhat subjective when it comes to confusion due to spectral arm overlaps. Here we defined a parameter, which is basically the zero-order flux ratio of the involved sources, that controls how low of an interfering overlap we allow with respect to contributing flux. The farther below unity this parameter is chosen to be, the more overlapping flux is excluded. This has to be done manually by adjusting this parameter until the HEG and MEG positive and negative first order fluxed spectra agree within their statistical uncertainties. Here it is mandatory that *all* four spectral arms agree. This then defines the exclusion criteria, i.e., the 'ignore' ranges in each spectral histogram.

Tab. 4 lists the total number of counts in the added HETG 1st orders after that cleaning procedure was applied and an effective exposure. The effective exposure shows how much of the original 2 Msec exposure remained for each source. In theory for bright sources such as θ^1 Ori A, C, E and MT Ori there should be little arm confusion. It turned out that this was only true for θ^1 Ori C mostly because it is so much brighter than any of the other sources. The other three sources suffered significant losses due to unfortunate observation roll angles which resulted in the situation that they confused each other. Here θ^1 Ori E interfered with θ^1 Ori C and A. The latter source suffered the most as it overlapped with three very bright sources, θ^1 Ori C, E and MT Ori. This situation was anticipated and minimized during observation planning by selecting more favorable roll angles. We also had over half a dozen cases where overlaps were so severe that at this point we could not recover any reasonable flux in the 1st orders. We note, that the method we apply here is likely over-cleaning the spectra, i.e. future refinements may improve these numbers, even recover 1st order counts in those sources that have zero counts and zero effective exposures in the present analysis.

In order to compare the resulting spectra with spectral models, the models must also ignore the same regions in the responses and sum to the cleaned observed counts. The rigorous way to do this would be to zero the corresponding channel range in the response matrix. However, since the response matrices for HETG dispersed orders are nearly diagonal, and since regions are randomly distributed throughout the count spectra, it is easier to modify the ARF in the same way as the counts. We can thus, for each order and grating type, add the counts, add the ARFs with exposure weighting, and use the RMF as is, to provide a merged set of data products suitable for further analysis. These data products, i.e. the cleaned merged spectra and their corresponding ARFs and RMFs, are available to the public and can be downloaded from the *Chandra* archive contributed data page[2] and alternatively from *Zenodo (XXXXX)*.

3. SOURCE DETECTION AND MASTER SOURCE LIST

3.1. *0th Order Source Detection*

The main field of view of Fig. 1 shows the merged zero order image of the ONC as observed with the *Chandra* HETG. We ran *wavedetect* on that field of view and compared the resulting source list with the COUP source list (Getman et al. 2005). Some of the sources in the COUP list were not detected, even though based on their brightness during the COUP campaign, they should have been detectable. The emphasizes the extreme flux variability young stars exhibit in X-rays.

3.2. *1st Order Source List*

We have accumulated a final master source list that emerged after all cleaning procedures. Of the 45 sources we found to be bright enough to produce good 1st order spectra and which are shown in Tab. 4, 36 sources survived the cleaning process described in Sec. 2.5 with well above several 1000 1st order counts. One source, θ^1 Ori C remained with over 2 Ms exposure after cleaning and 25 sources have between 1 and 2 Ms exposures. The smallest exposure is for COUP 662 with 750 ks. 24 sources yield over 10 000 1st order counts, 11 sources have more than 5000 counts, only 2 sources are below that number. Nine sources were excluded because their spectra had less than a few 100 counts left after cleaning. These sources are fainter than the rest and we anticipate that future improvements in the cleaning procedure may recover some more counts.

As expected, all bright sources were detected by COUP (Feigelson et al. 2005) and Tab. 4 provides the COUP numbers of the object as well as the coordinates as provided by COUP (Getman et al. 2005). The table also provides some physical parameters describing each source which were collected from previous optical studies (Hillenbrand 1997; Herbig & Griffin 2006; Da Rio et al. 2010; Hillenbrand et al. 2013; Maíz Apellániz

[2] https://space.mit.edu/HETG/Orion/orion_spectra_lcs_r1_test1.html

Table 4. HETGS 1ST Order Master Source Table (Data available in mashine readable table (MRT))

Star	RA	DEC	Spectral	T$_{eff}$	Mass	log(age)	COUP	1st order	eff. exp
	[h m s]	[d m s]	Type	[kK]	[$M_\odot$]	[yr]	[#]	[counts]	[ks]
θ^1 Ori C	5 35 16.46	-5 23 22.8	O7V	44.6	35		809	1033433	2085
θ^2 Ori A	5 35 22.90	-5 24 57.8	O9.5IV	30.9	25		1232	19573	1445
θ^1 Ori A	5 35 15.83	-5 23 14.3	B0.5Vp	28.8	15		745	71578	1276
θ^1 Ori B	5 35 16.14	-5 23 06.8	B3V		7		778	0	0
θ^1 Ori E	5 35 15.77	-5 23 09.9	G2.5	14.8	2.8		732	131865	1592
θ^1 Ori D	5 35 17.26	-5 23 16.6	B1.5Vp	32.4	16	<6.39	869	0	0
θ^2 Ori B	5 35 26.40	-5 25 00.8	B0.7V	29.5	15	<6.30	1360	0	0
MV Ori	5 35 18.67	-5 20 33.7	F8-G0	5.24	2.72	6.17	985	17368	1189
TU Ori	5 35 20.22	-5 20 57.2	F7-G2	5.90	2.43	5.55	1090	9813	1027
V2279 Ori	5 35 15.93	-5 23 50.1	G4-K5	5.24	2.37	6.12	758	16545	1058
V348 Ori	5 35 15.64	-5 22 56.5	G8-K0	5.24	2.33	6.23	724	34731	1236
V1399 Ori	5 35 21.04	-5 23 49.0	G8-K0	5.11	2.28	6.17	1130	32765	1816
V1229 Ori	5 35 18.37	-5 22 37.4	G8-K0	5.24	2.22	6.14	965	28267	1349
V2299 Ori	5 35 17.06	-5 23 34.2	K0-K7	5.11	2.08	6.27	855	10640	905
LR Ori	5 35 10.51	-5 26 18.3	K0-M0	5.24	2.05	6.43	387	9549	1193
2MASS3	5 35 17.22	-5 21 31.7	K4-K7	4.68	1.97	5.56	867	7024	942
MT Ori	5 35 17.95	-5 22 45.5	K2-K4	4.58	1.99	5.39	932	150965	1701
LU Ori	5 35 11.50	-5 26 02.4	K2-K3	4.78	1.86	6.07	430	13386	1259
V1338 Ori	5 35 20.17	-5 26 39.12	K0-G4	5.25	1.83	6.32	1087	0	0
Par 1841	5 35 15.18	-5 22 54.53	K6-G4	5.25	1.83	6.74	682	0	0
V1333 Ori	5 35 17.00	-5 22 33.0	K5-M3	4.95	1.68	6.32	854	13484	918
V2336 Ori	5 35 18.70	-5 22 56.8	K0-K3	4.79	1.65	6.50	993	0	0
Par 1842	5 35 15.27	-5 22 56.8	G7-G8	5.56	1.56	6.62	689	15783	941
V1330 Ori	5 35 14.90	-5 22 39.2	K5-M2	4.58	1.47	5.88	670	21357	1314
Par 1837	5 35 14.99	-5 21 59.93	K3.5	4.58	1.47	6.30	669	6956	1096
Par 1895	5 35 16.38	-5 24 03.35	K4-K7	4.00	0.91	5.59	801	5724	838
V1279 Ori	5 35 16.76	-5 24 04.3	M0.9e	4.20	0.91	5.84	828	13683	1251
V491 Ori	5 35 20.05	-5 21 05.9	K7-M2	3.99	0.74	5.92	1071	18586	1380
Par 1839	5 35 14.64	-5 22 33.70	K7	3.99	0.74	5.30	648	6382	877
LQ Ori	5 35 10.73	-5 23 44.7	K2	3.90	0.70	3.99	394	34093	1617
V1326 Ori	5 35 09.77	-5 23 26.9	K4-M2	3.90	0,64	5.76	343	17530	1402
COUP 1023	5 35 19.21	-5 22 50.7	K5-M2	4.40	0.62	6.36	1023	6119	815
V495 Ori	5 35 21.66	-5 25 26.5	M0	3.80	0.58	6.43	1161	13126	1453
V1527 Ori	5 35 22.55	-5 23 43.7	M0	3.80	0.57	6.43	1216	0	0
V1228 Ori	5 35 12.28	-5 23 48.0	K1-M0	3.80	0.56	5.95	470	9440	1133
V1501 Ori	5 35 15.55	-5 25 14.15	K4-M1	3.80	0.55	4.65	718	16384	1564
2MASS4	5 35 23.81	-5 23 34.3	M1e	3.72	0.47	6.21	1268	0	0
V1496 Ori	5 35 13.80	-5 22 07.02	K2e	3.43	0.39	5.16	579	6425	1040
2MASS1	5 35 09.77	-5 21 28.3	M3.5	3.31	0.28	6.52	342	13960	1581
COUP 450	5 35 11.80	-5 21 49.3	M4.4	3.16	0.22	6.47	450	24771	1642
Par 1936	5 35 19.30	-5 20 07.9	K2	4.95	1.4	6.78	1028	4301	959
V1230 Ori	5 35 20.72	-5 21 44.3	B1	18.6	6.4		1116	24363	1507
COUP 662	5 35 14.90	-5 22 25.41					662	4026	750
JW 569	5 35 17.95	-5 25 21.24	M3.5	3.16	0.1		936	0	0
V1398 Ori	5 35 13.45	-5 23 40.43	M0				545	7068	980

Table 5. Multiplicity and components of θ^1 Ori and θ^2 Ori

Star	Comp.	SpT	Mass $[M_\odot]$	Separation [AU]
θ^1 Ori A –	1	B0.5Vp	15	
	2		≈ 4	100
	3		≈ 2.6	0.71
θ^1 Ori B –	1	B3V	7	
	2		≈ 4	382
	3		≈ 3	49
	4		≈ 1	248
	5		≈ 2	0.12
	6		≈ 2	5
θ^1 Ori C –	1	O7V	35	
	2		9	18.1
	3		≈ 1	0.41
θ^1 Ori D –	1	B1.5Vp	16	
	2		≈ 1	580
	3		≈ 6	0.77
θ^1 Ori E –	1	G2.5	2.8	
	2		2.8	0.09
θ^2 Ori A –	1	O9.5IV	$\simeq 25$	
	2		≈ 10	0.42
	3		≈ 10	157
θ^2 Ori B –	1	B0.7V	15	
	2		≈ 1.6	40

References—References: Preibisch et al. (1999), Kraus et al. (2009), Grellmann et al. (2013), Karl et al. (2018), Maíz Apellániz et al. (2022)

et al. 2022). In fact the table itself is approximately sorted by modeled stellar masses, even though for some stars we could not find model predictions.

All of the early (O and B) type stars in our sample are known to be multiple systems (see Petr et al. 1998; Preibisch et al. 1999; Grellmann et al. 2013; Karl et al. 2018, and references therein). Table 4 lists only the properties of the primary component, but a summary of the companion properties is provided in Tab. 5.

3.3. *Gaia Distances of the ONC and Our Stellar Sample*

Thanks to Gaia parallaxes, the distance to the Orion Nebula Cluster is very well known today. In the recent study of (Maíz Apellániz et al. 2022) based on the Gaia DR3 data, a distance of $D = (390 \pm 2)$ pc was determined for a sample of astrometrically selected cluster members.

Although it is highly likely that the X-ray selected stars in our Master Source List are ONC members, the X-ray detection alone does not immediately prove that this star is actually a young star in the Orion Nebula Cluster; there may be some level of contamination by foreground and background objects.

In order to check this, we obtained the parallaxes for the stars in our Master Source List from the Gaia DR3 archive. Parallaxes were found for 43 of the 45 stars in our Master Source List; the two exceptions are COUP 450 and COUP 662. We performed the bias-correction of the parallaxes with the algorithm described in Lindegren et al. (2021).

All parallaxes are approximately in the expected range for ONC members around $\varpi \approx 2.5$ mas and there are no immediately obvious foreground or background objects in the sample. However, the parallaxes show (of course) some scatter, and there are four stars (V2299 Ori, V1279 Ori, LQ Ori, and Par 1936) for which the 3σ uncertainty range for their parallax (i.e., $\varpi \pm 3\,\sigma_\varpi$) does not include the expected value, which, in principle, qualifies them as "outlier candidates". However, in all four cases the "Renormalised Unit Weight Error" (RUWE) associated to the Gaia data of these stars is high (> 1.4). The RUWE value is a goodness-of-fit statistic describing the quality of the astrometric solution (see Lindegren 2018), and RUWE values above 1.4 indicate a low reliability of the astrometric parameters (Fabricius et al. 2021).

We determined the most likely distance to the sample of stars in our Master Source List with a Bayesian inference algorithm, employing the program *Kalkayotl* (Olivares et al. 2020). *Kalkayotl* is a free and open code that uses a Bayesian hierarchical model to obtain samples of the posterior distribution of the cluster mean distance by means of a Markov chain Monte Carlo (MCMC) technique implemented in PyMC3. *Kalkayotl* also takes the parallax spatial correlations into account, which improves the credibility of the results, and allows to derive trustworthy estimates of cluster distances up to about 5 kpc from Gaia data (Olivares et al. 2020).

We used *Kalkayotl* version 1.1. For the prior, we used the implemented Gaussian model with a mean distance of $D_{\rm prior} = (390 \pm 10)$ pc and a cluster scale of $S_{\rm prior} = 10$ pc. The calculations were done in distance space, and the reported uncertainties for the inferred mean distances are the central 68.3% quantiles (corresponding to the "$\pm 1\sigma$ range" for a Gaussian distribution).

For the complete sample of 43 stars with parallaxes we obtained a distance of 396.5 pc with an uncertainty range of [391.8 , 401.2] pc. Excluding the above mentioned four "outlier candidates", the result changes only very slightly to 395.9 pc with an uncertainty range of [392.9 , 398.9] pc. These distance values for our sample are well consistent with the above mentioned distance determination for the ONC.

4. GLOBAL HETG PROPERTIES

4.1. *Light Curves and Flares*

The field of the Orion VLP observations includes a wealth of sources that vary in brightness with time. Many of the sources are late-type stars that can flare. Fig. 3 (on-line version only) also shows a video that gives a full appreciation of variability in this field. The video was created from the merged evt2 event file of all 70 obsids, split equally into 1000 frames. Therefore, each frame is a subsample of an obsid. Every source in the images that varies can be investigated in the future.

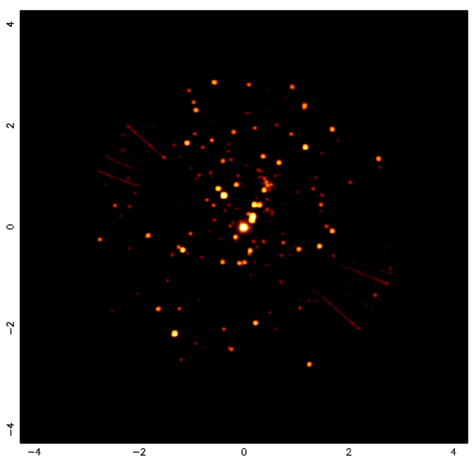

Figure 3. Example image of the Orion Nebula Cluster for approximately 3' around $\theta^1 OriC$. This image represents 10% of the exposure time on this field during the 2018-2019 campaign. The associated video shows frames with 0.1% of the exposure time in sequential order, organized into a movie to highlight the remarkable short-term variability of the sources in this region.

We investigated the variability of each of the 45 sources using the Gregory-Lorado variability index. The variability index is determined using the algorithm of Gregory & Loredo (1992), as implemented in CIAO as *glvary*, and is based on the probability that the count rate of the source is not constant during the observation, using a comparison of binned event arrival times. This index is normally used only within an individual observation, but can also be used for merged data if the Good Time Intervals are properly handled. According to Rots (2012), if the source has a variability index of 0-3, it is not considered variable within the observation. A variability index of 8 or above is definitely variable. To examine the variability of each source, a merged file of all non-confused observations taken between 2019 and 2020 was created (see Tables 2 and 3 for list of observations). *glvary* was used to evaluate the variability index for this set of recent non-confused observations for each source. We find that all sources are definitely variable with a variability index of 9-10, except for COUP 1023 which is possibly variable and θ Ori D and V1527 Ori which are not variable. Examples of the light curves produced by the merged observation file are shown in Figs. 4 and 5. The time gaps between the individual observations have been eliminated in these plots and the light curves display the data as if they were one long continuous observation for each source.

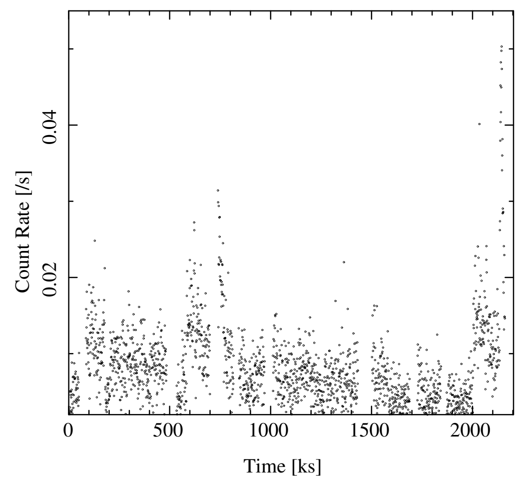

Figure 4. Concatenated light curve for 2019-2020 V1230 Ori observations, each in 1 ksec bins. Time on x-axis is cumulative exposure since the start of the first observation plotted. Data for obsids where confusion affects the zeroth order have been eliminated in the plot.

In addition to the primary 45 sources, the variability index of about 1600 additional sources in the fields are being calculated.

The analysis of flares in later type stars is an important component of the Orion VLP program. The ultimate goal is to analyze the high resolution spectra near the times of flares to obtain detailed information about the spectral parameters both before and after the flares. A follow-on paper will describe in detail the method for eliminating confused zeroth order sources and give quantitative information on the variability methods used.

4.2. *HETG 1st Order Spectra and Background*

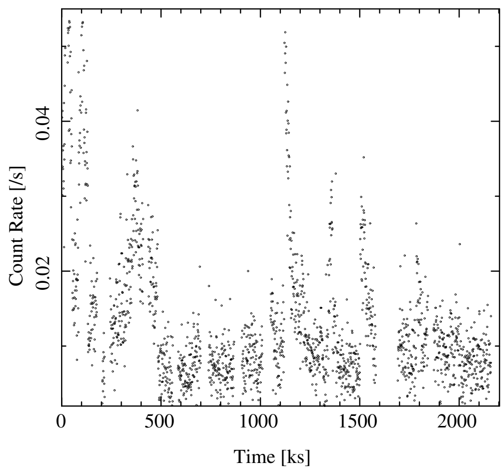

Figure 5. Concatenated light curve for 2019-2020 LQ Ori observations, each in 1 ksec bins. Time on x-axis is cumulative exposure since the start of the first observation plotted. Data for obsids where confusion affects the zeroth order have been eliminated in the plot.

The sample of 36 sources that passed the cleaning process contains four massive ($> 6\ M_\odot$) stars, about a dozen intermediate mass ($\sim 2-3\ M_\odot$) stars, and about twenty low-mass ($< 2\ M_\odot$) stars (see Table 4). The modeling of the spectra and the X-ray line emission is done in various steps. One item is selective bandpass. The bright sources as observed in the early phases of the *Chandra* mission also have low absorption and provide significant flux above 16 Å. Observations in cycles later than Chandra Cycle 16 have too much contaminant absorption to allow for much flux above 16 Å. Thus we allow a wider bandpass for bright sources analysed in the early *Chandra* Cycles up to 22 Å, while limiting the bandpass for sources otherwise to 16 Å. The model spectra apply the Astrophysical Database Emission Database (APED) to fit collisionally ionized emissions to the spectra. The number of temperature components mostly depends on the need to cover the available wavelength range but also depends on the strength of the recorded X-Ray continuum. As for the fitting procedure we applied a number of APED temperature components plus background (see below) with all APED fit parameters active as a pre-fit step. In this overview analysis we are not interested in all the details and we then fixed the APED abundance values to the pre-fit result. In a second step we then used the ISIS function `conf_loop` to determine 90% uncertainty values of the absorption column N_H, the involved temperatures kT_i, where i is the APED component index, and the emission measures EM_i of each each component.

Most of the stars in the sample are fainter than a few 10^{-13} erg cm^{-2} s^{-1} and thus require the inclusion of an X-ray background which becomes significant at soft X-rays. This background consists mainly of an HETG/ACIS-S instrumental component[3] with some contribution of a flat diffuse stellar background from weak off-axis sources from the outer regions of the ONC cluster. Given that we have so many roll angles involved in the available 70 observations, this background should be fairly isotropic for all sources. The sample contains over half a dozen of absorbed sources where we can directly determine this background contribution. Figure 6 shows the example of COUP 450. It is heavily absorbed and the hard X-ray bandpass below 9 Å is fitted by a single APED temperature function, while the soft part directly shows this background. It is a powerlaw of photon index 6.5 with a normalization of 6.068×10^{-5} photons cm^{-2} s^{-1}. We tested this function with half a dozen absorbed sources with powerlaw parameters agreeing within 5%. We then added this powerlaw to every spectral fit procedure. This rising tail beyond 13 Å is well predicted by the empirically measured instrumental background.

4.3. *Massive Stars*

There are four massive stars in the sample, the two most massive are θ^1 Ori C (O7 V) and θ^2 Ori A (O9.5 IV), plus two less massive stars θ^1 Ori A and V1230 Ori. Even though all of these stars are bright with respect to the HETG background, we include this background in all the fits. Except for V1230 Ori, some early *Chandra* HETG results have been published before on all the other massive stars (Schulz et al. 2000, 2003; Gagné et al. 2005; Mitschang et al. 2011). Here we assess how the new 2.2 Msec data can serve to provide new insights.

4.3.1. θ^1 *Ori C*

The most massive component of the Trapezium cluster is the triple system θ^1 Ori C, comprised of a $\sim 33M\odot$ oblique magnetic rotator θ^1 Ori C1, a $\sim 1\ M_\odot$ star C3 at only ≈ 0.04 AU (GRAVITY Collaboration et al. 2018, and references therein), and a $\sim 10\ M_\odot$ star C2 at 16.7 AU, with an orbital period of 11.26 years (Rzaev et al. 2021).

The cleaning procedure left about 95% of the exposure for θ^1 Ori C intact, yielding a total exposure time of 2.085 Msec in 68 OBSIDs. The X-ray source is very

[3] For details, see the *Chandra* Proposers' Observatory Guide §8.2.3 (https://cxc.harvard.edu/proposer/POG/html/chap8.html#tth_sEc8.2.3) and memo referenced therein.

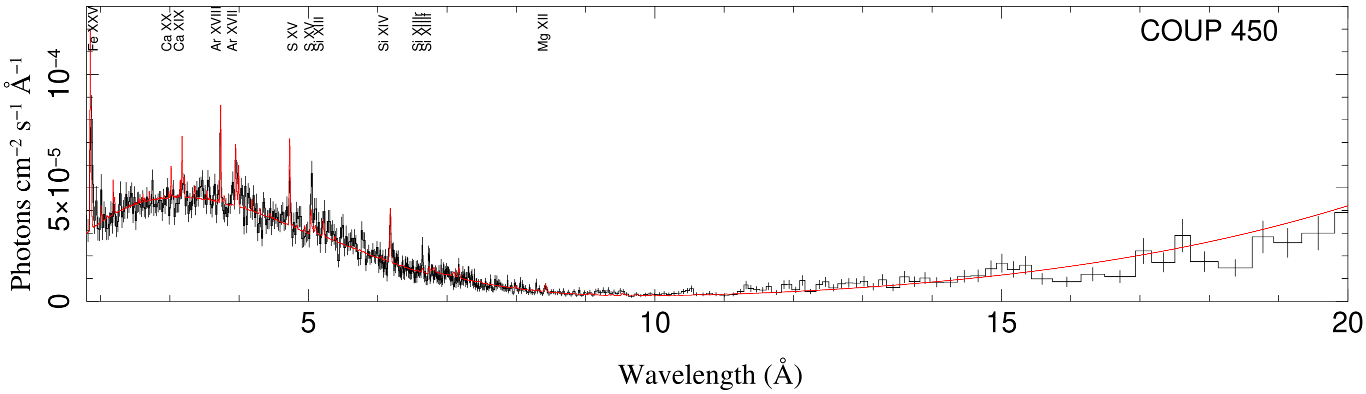

Figure 6. Absorbed one-component plasma fit with a model background for COUP 450. The background has a power law shape and becomes noticeable above 10 Å and dominant above 16 Å; it is primarily due to local instrumental background.

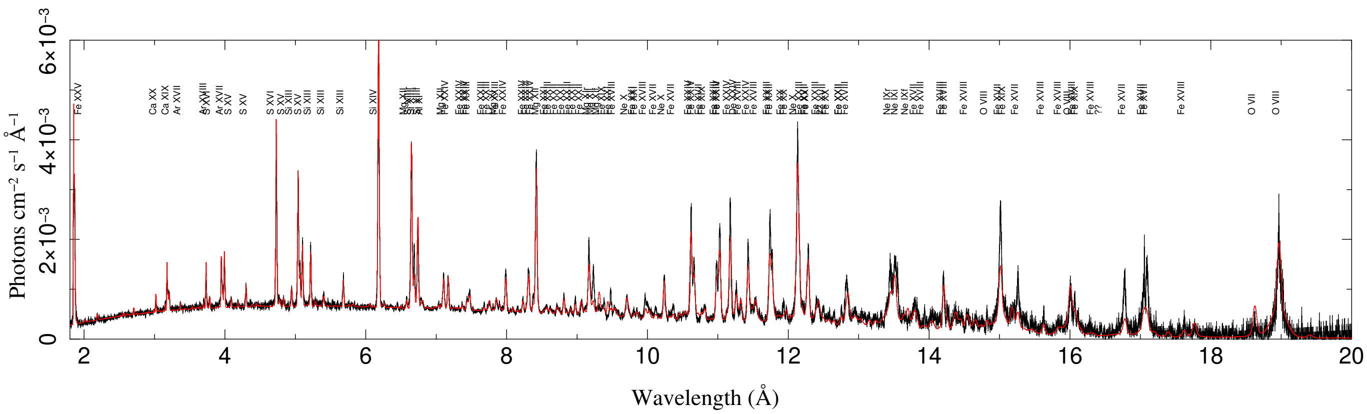

Figure 7. The broadband 2.1 Msec spectrum of θ^1 Ori C with line labels. The spectrum shows over 100 detected lines at high signal to noise.

bright with an average unabsorbed $0.5-8.0$ keV X-ray flux of 4.0×10^{-11} erg s^{-1} cm^{-2}, and an average X-ray luminosity $L_X \approx 7.7 \times 10^{32}$ erg s^{-1} at 410 pc. The high-signal-to-noise HEG and MEG spectra were analyzed using a bin size as low as 0.005 Å over the 1.65 Å to 23 Å bandpass. While still very good, count statistics decline towards larger wavelengths due to interstellar absorption, and the worsening low-energy response of the ACIS-S detector. In fact, including data sets obtained after 2007 does not improve signal-to-noise above 16 Å. Fig. 7 shows the combined, first-order HEG/MEG spectrum of θ^1 Ori C, exhibiting hundreds of X-ray lines in over seventy individual line complexes.

A preliminary fit of the spectra was performed using 5 APED temperature components. The X-ray temperatures range between 8 and 32 MK, basically similar to results reported by Schulz et al. (2003). While the overall fit was acceptable, residuals indicate that more detailed line profile analysis will be necessary. However it is interesting to note that this preliminary fit of the long exposure spectrum did not require overly hot temperature components, we stress, though, that for this more precise line profile fits need to be preformed. For this demonstration we restrict the analysis to fit generic Gaussian line profiles to selected bright lines in order to determine the order of magnitude of the velocity broadening in the resolved lines. We find that the lines are resolved with very moderate broadening of about 300 km s^{-1}. Specifically we find 369 ± 16 km s^{-1} for Ne X, 279 ± 8 km s^{-1} for Mg XII, 326 ± 8 km s^{-1} for Si XIV, 381 ± 26 km s^{-1} for S XVI, and 318 ± 52 for Ar XVIII. The consistency of these values over a large wavelength range as well as the small uncertainties are a reflection of the superb properties of this data set.

A detailed line-by-line analysis of the phase-resolved X-ray spectra will be presented by Gagné et al. (2024, in preparation). Numerical 3D modeling of the magnetically confined wind shocks will be presented by Subramanian et al. (2024, in preparation).

The high significance in the emission lines in the 1st order of θ^1 Ori C allows the analysis of the spectral properties at the highest possible spectral resolution with nearly perfect statistics throughout the entire waveband between 1.7 and 23 Å. One example where these conditions benefit this analysis are the He-like triplets in this bandpass. Fig. 8 on the left side shows the triplets from

Mg, Si, S, Ar, Ca, and Fe at no data binning. The statistical 1σ errors are plotted as well but so small that they are not visible. Previous HETG studies of the source (Schulz et al. 2000, 2003; Gagné et al. 2005) showed that the lines are well resolved with a FWHM of a few hundred km/s.

The combination of high resolution and good count statistics should prove invaluable for magnetic wind shock model analysis. However at 1st order resolution spectral details of the triplets start to fade past Si, i.e. the line components of higher Z triplets are not fully resolved. Here this long exposure allows the utilization of the higher orders of the transmission gratings, specifically the MEG 3rd and HEG 2nd orders which features each nearly 10% of the 1st order efficiency. Fig. 8 on the right shows He-like triplets at this higher resolution. The 1σ statistical error bars are now clearly visible due to the reduced efficiency of the higher orders. However, the main triplet components are now resolved up to Ca and partially at Fe. The resolving power at Mg XI is now 1480, at Si XIII is 1000, at s XV is 820, at Ar XVII is 640, at Ca XIX is 515 and at Fe almost 310, which are the highest resolving powers in He triplets to date.

4.3.2. *Others*

The three other massive stars in the sample are θ^1 Ori A, θ^2 Ori A and V1230 Ori. For the latter two stars the cleaning procedure leaves about 1.5 Msec of remaining exposure, while for θ^1 Ori A the exposure is 1.2 Msec. This lower exposure is caused by the combination of this star being very close to θ^1 Ori C and a period of unfortunate roll angle of the telescope which caused more confusion of the two stars. In both cases we harvest several 10^4 cts in the bandpass between 1.7 Å and 20 Å.

There are three more massive stars in the sample for which we could not harvest valid counts in the HETG 1st orders. The most prominent example is θ^1 Ori D, which is optically supposed to be very close to θ^1 Ori A, but not only do we have a large amount of confusion with other Trapezium stars, the star appears to be also very dim in X-rays, i.e. it is hardly detected even in the 0th order. The similarity of these stars is striking, as their massive components have very similar mass, and both stars have two low- and intermediate mass companions (see Tab 5). The absence of X-ray detection can have two reasons, one is that its spectrum is very soft and suffers from ACIS filter absorption, another is that it is inherently X-ray weak. Both explanations are at odds with the appearance of θ^1 Ori A. Specifically the fact that θ^1 Ori D has lower mass companions but no significant coronal emissions are detected is quite puzzling.

The other massive stars are θ^1 Ori B and θ^2 Ori B. According to Tab 5, θ^1 Ori B is a cluster of at least six stars, mostly of intermediate mass. The cluster is detected in 0th order but we do no have HETG 1st order spectra. The same is true for θ^2 Ori B, which is well detected in 0th order but no significant emissions could be recovered in HETG 1st order.

4.4. *Intermediate- and Low-Mass Stars*

There are 11 stars of masses between 1.5 $M_\odot$ and 3 $M_\odot$ in the sample, which we designate as intermediate mass stars and 20 stars below 1.5 $M_\odot$, which we designate as low-mass stars. This designation is somewhat arbitrary but helps in the discussion of their properties. In the analysis we treat them similar as coronal sources and apply the same model to their data. This model consists of the standard soft background, column density and two APED temperature components. We first employ a pre-fit step between 1.7 Å and 22 Å in which we keep all parameters except for the pre-determined background and the X-ray line widths. For the line profiles we apply delta functions which allows for the fit to apply the pure HETG line response functions with no intrinsic broadening. We do not expect significant line broadening in coronal sources and this step helps stabilize the fit procedure. Specifically in very hot temperature components where there are no or only a few lines, free line widths tend to artificially broaden and contribute to the continuum. However, in a separate step we perform individual line fits on the Ne X and Si XIV in all sources where they are detected. After the pre-fit we then fix the abundances and apply the *confloop* function to further fit column density, APED normalisations and temperatures and determine the 90% uncertainties. The final results of these fits are shown in Table 6.

4.4.1. *Surface Flux*

The global fits result in X-ray fluxes of a few 10^{-13} erg cm^{-2} s^{-1} for all sources except MT Ori, which is an order of magnitude brighter. In order to determine what we call surface flux we calculate the source luminosity from the measured unabsorbed flux and divide by the surface area of the star. The radius of each star is calculated from the bolometric luminosity and the effective surface temperature, which are measured quantities and listed in the standard COUP tables.

In Fig. 9 we plot the surface flux versus the age of the cluster source as listed in Tab. 4. These ages are also taken from the COUP tables and even though not very well known they allow global order of magnitude comparisons. The COUP radii are also subject to systemat-

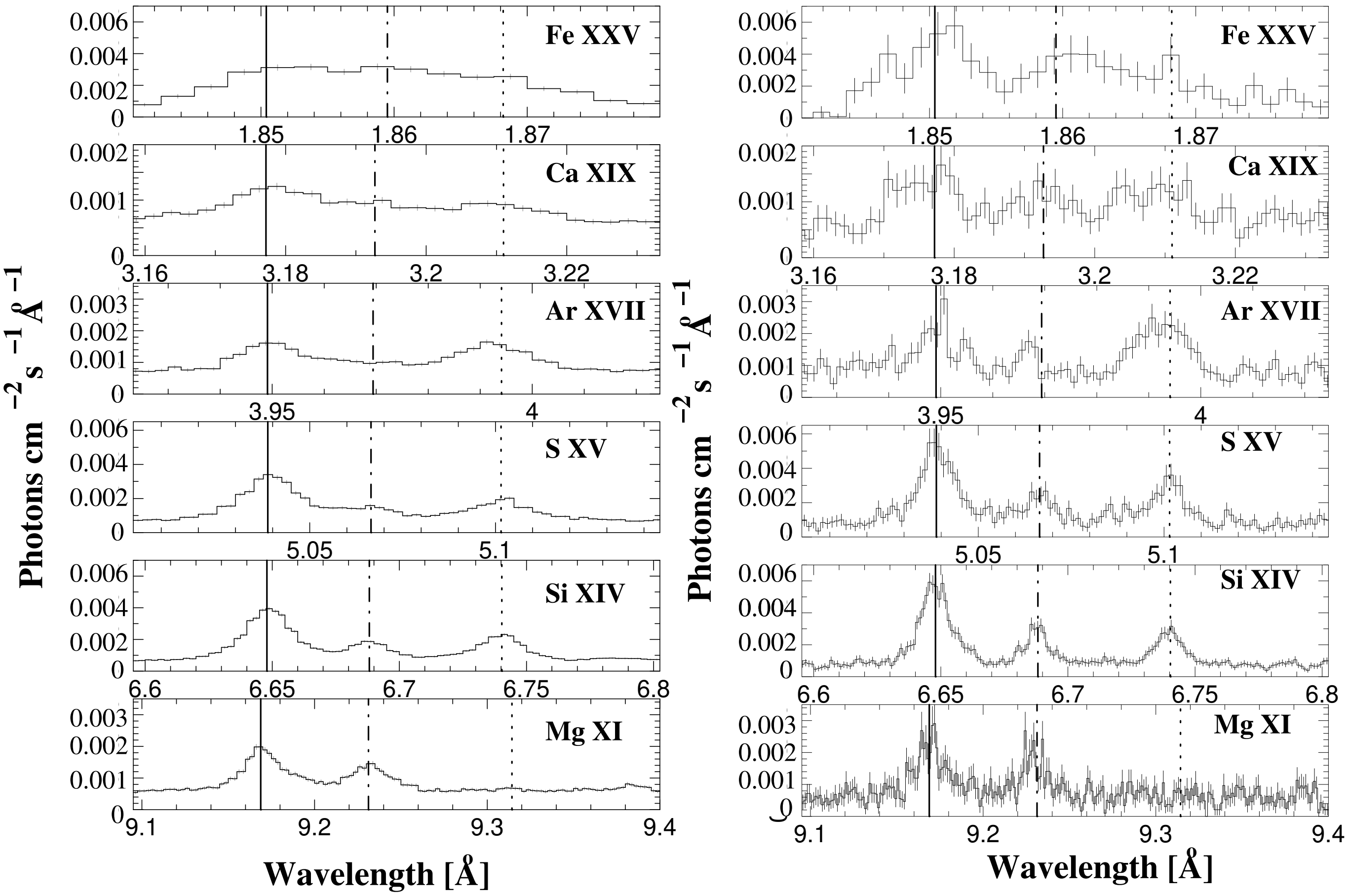

Figure 8. Here we show He-like triplets of Mg, Si, S, Ar, Ca and Fe in various orders for θ^1 Ori C. On the left are the triplets in 1st order, on the right the ones in higher orders, MEG 3rd and HEG 2nd orders. While the 1st orders provide high signal to noise power, the significantly higher resolving power of the higher grating orders provide much more details.

ical uncertainties and we added a 10% contribution to the uncertainty of the surface flux. The plot shows that similar age stars have similar surface fluxes. There may be a possible trend of increasing (coronal) X-ray surface brightness with PMS age. Such a trend would seem to be consistent with studies of the evolutionary behavior of TTS X-ray emission dating at back to Kastner et al. (1997) in the TW Hydra Association. There are two exceptions. V495 Ori exhibited a giant flare that lasted only for a week; V491 Ori is a highly absorbed persistent source that will need special attention.

4.4.2. *Absorption Column Densities*

The global fits resulted in column densities N_H between a few times 10^{21} cm^{-2} and a few times 10^{22} cm^{-2}. The largest column was observed in COUP 450 with 1.3×10^{22} cm^{-2}. LQ Ori exhibits the lowest column consistent with a value below 10^{20} cm^{-2}. The column density towards the ONC is estimated to be $\sim 2.3 \times 10^{21}$ cm^{-2} (see discussion in Schulz et al. 2015) which implies most of the excess absorption observed is likely intrinsic to the stellar systems. In Fig. 10 we plot the measured X-ray absorption column versus the optical extinction.

The figure also shows other young stars from the literature for comparison. The sample of Günther & Schmitt (2008) concentrates on stars that are observed with high-resolution X-ray spectroscopy similar to our sample from the ONC. The figure also displays two stars where the absorbing column density and the optical extinction have been observed to change with time, in particular in TWA 30A (Principe et al. 2016) and AA Tau (Grosso et al. 2007; Schneider et al. 2015). Green lines indicate $N_{\rm H}/A_V$ ratios from the ISM and two star forming regions from Vuong et al. (2003); for the ONC those authors have only a very small sample with large uncertainties that appears compatible with the ISM.

To provide an independent means of estimating N_H, we compared the flux in the Ne X alpha line with the flux in the Ne X beta line. The Ne X lines are relatively strong in the spectra of our sources and the wavelength separation of the alpha and beta lines is adequate to estimate N_H. We were able to make this estimate

Table 6. HETG Spectral Parameters of 2 Temperature APED fits (Data available in mashine readable table (MRT)):

Star	N_H (1)	T_1 (2)	T_2 (2)	EM_1 (3)	EM_2 (3)	v_{Ne} (4)	v_{Si} (4)	f_x (5)	L_x (6)
MV Ori	$10.10^{0.56}_{0.55}$	$13.81^{0.65}_{0.67}$	$90.00^{0.00}_{19.17}$	$2.25^{0.17}_{0.05}$	$0.72^{0.11}_{0.04}$	153^{96}_{227}	986^{202}_{61}	$4.6^{4.9}_{4.4}$	1.1
TU Ori	$9.20^{1.50}_{0.43}$	$15.67^{2.27}_{1.62}$	$69.09^{13.91}_{16.47}$	$1.04^{0.16}_{0.18}$	$0.56^{0.16}_{0.15}$	319^{410}_{220}	646^{484}_{597}	$2.6^{2.7}_{2.4}$	0.6
V2279 Ori	$5.43^{0.49}_{0.50}$	$9.18^{1.09}_{1.02}$	$45.61^{3.52}_{3.38}$	$0.93^{0.17}_{0.16}$	$1.50^{0.10}_{0.09}$	115^{269}_{115}	374^{257}_{167}	$4.9^{5.1}_{4.7}$	1.1
V348 Ori	$2.55^{0.25}_{0.23}$	$10.27^{0.70}_{0.71}$	$41.10^{1.66}_{1.53}$	$0.61^{0.10}_{0.09}$	$2.80^{0.08}_{0.08}$	209^{24}_{95}	258^{98}_{258}	$9.4^{9.9}_{8.9}$	1.9
V1229 Ori	$2.76^{0.28}_{0.28}$	$9.61^{0.78}_{1.19}$	$35.15^{1.31}_{1.53}$	$0.56^{0.08}_{0.09}$	$2.47^{0.07}_{0.12}$	153^{58}_{123}	679^{455}_{380}	$5.7^{6.0}_{5.5}$	1.2
V1399 Ori	$3.14^{0.36}_{0.24}$	$9.70^{0.73}_{0.76}$	$31.33^{1.16}_{1.19}$	$0.62^{0.12}_{0.09}$	$2.20^{0.09}_{0.08}$	257^{64}_{50}	268^{121}_{189}	$7.3^{7.7}_{7.0}$	1.5
V2299 Ori	$10.58^{0.84}_{0.73}$	$16.83^{2.96}_{2.71}$	$57.82^{19.51}_{10.68}$	$0.81^{0.18}_{0.55}$	$1.23^{0.45}_{0.17}$	219^{85}_{103}	218^{267}_{218}	$4.4^{4.6}_{4.2}$	1.0
LR Ori	$4.09^{0.82}_{0.74}$	$12.00^{0.87}_{1.55}$	$60.00^{11.00}_{10.53}$	$0.57^{0.13}_{0.14}$	$0.51^{0.25}_{0.03}$	213^{112}_{99}	179^{221}_{179}	$1.9^{2.0}_{1.8}$	0.4
2MASS3	$5.10^{0.84}_{0.80}$	$14.46^{1.11}_{1.32}$	$74.60^{15.40}_{17.00}$	$0.36^{0.40}_{0.03}$	$0.57^{0.09}_{0.09}$	153^{122}_{50}	50^{112}_{373}	$1.6^{1.7}_{1.5}$	0.4
MT Ori	$3.38^{0.12}_{0.11}$	$12.35^{0.78}_{0.64}$	$40.95^{0.96}_{8.17}$	$1.37^{0.22}_{0.17}$	$9.96^{0.17}_{0.22}$	195^{27}_{24}	289^{58}_{89}	$34.5^{0.8}_{1.7}$	7.2
LU Ori	$4.45^{0.63}_{0.64}$	$10.96^{0.49}_{0.48}$	$45.35^{4.58}_{3.97}$	$0.68^{0.15}_{0.14}$	$0.77^{0.06}_{0.06}$	322^{87}_{134}	470^{213}_{181}	$2.6^{2.7}_{2.4}$	0.6
V1333 Ori	$9.29^{0.58}_{0.60}$	$12.04^{0.61}_{0.75}$	$30.39^{2.57}_{2.60}$	$1.52^{0.25}_{0.27}$	$1.30^{0.20}_{0.15}$	222^{87}_{208}	636^{635}_{260}	$3.3^{3.5}_{3.2}$	0.7
Par 1842	$1.77^{0.43}_{0.37}$	$10.82^{0.93}_{1.07}$	$36.39^{2.14}_{2.19}$	$0.45^{0.11}_{0.10}$	$1.52^{0.09}_{0.08}$	216^{31}_{138}	556^{276}_{341}	$4.3^{4.5}_{4.1}$	0.9
V1330 Ori	$4.95^{0.45}_{0.40}$	$10.46^{0.74}_{0.47}$	$43.05^{3.08}_{4.95}$	$0.65^{0.13}_{0.11}$	$1.57^{0.07}_{0.08}$	152^{176}_{108}	254^{124}_{253}	$5.3^{5.6}_{5.0}$	1.1
Par 1837	$5.45^{0.37}_{0.84}$	$7.22^{1.44}_{1.49}$	$45.03^{4.66}_{5.42}$	$0.35^{0.21}_{0.09}$	$0.52^{0.06}_{0.04}$	321^{140}_{138}	597^{288}_{326}	$1.5^{1.6}_{1.4}$	0.3
Par 1895	$0.05^{0.27}_{0.04}$	$13.13^{1.93}_{1.31}$	$64.33^{15.71}_{9.72}$	$0.18^{0.05}_{0.04}$	$0.39^{0.04}_{0.05}$	318^{290}_{156}	253^{99}_{89}	$1.5^{1.5}_{1.4}$	0.3
V1279 Ori	$2.02^{0.58}_{0.40}$	$9.58^{0.92}_{1.08}$	$38.34^{2.67}_{2.52}$	$0.26^{0.10}_{0.07}$	$0.92^{0.05}_{0.07}$	279^{55}_{132}	247^{101}_{199}	$2.7^{2.8}_{2.5}$	0.5
V491 Ori	$16.21^{0.91}_{0.50}$	–	$43.40^{2.23}_{3.08}$	–	$2.69^{0.06}_{0.10}$	–	400^{358}_{220}	$7.7^{8.1}_{7.3}$	1.8
Par 1839	$2.99^{0.86}_{0.84}$	$11.67^{1.00}_{1.22}$	$81.22^{8.78}_{11.71}$	$0.48^{0.11}_{0.11}$	$0.43^{0.06}_{0.03}$	269^{88}_{164}	278^{200}_{277}	$1.9^{2.0}_{1.8}$	0.4
LQ Ori	$0.29^{0.20}_{0.23}$	$10.52^{0.36}_{0.31}$	$34.28^{2.16}_{1.32}$	$0.68^{0.11}_{0.07}$	$1.89^{0.15}_{0.30}$	213^{31}_{29}	221^{160}_{220}	$5.0^{5.3}_{4.8}$	1.0
V1326 Ori	$3.19^{0.41}_{0.44}$	$6.04^{0.55}_{0.50}$	$29.46^{1.56}_{1.21}$	$0.98^{0.21}_{0.18}$	$1.27^{0.06}_{0.06}$	191^{39}_{59}	301^{188}_{194}	$2.7^{2.8}_{2.6}$	0.6
COUP 1023	$5.56^{1.34}_{1.13}$	$18.96^{3.09}_{2.95}$	$78.00^{12.00}_{14.96}$	$0.60^{0.13}_{0.13}$	$0.28^{0.11}_{0.04}$	86^{83}_{78}	243^{193}_{145}	$1.7^{1.8}_{1.6}$	0.4
V495 Ori	$5.24^{0.72}_{0.69}$	$11.61^{1.47}_{1.01}$	$69.02^{14.58}_{9.43}$	$0.51^{0.12}_{0.11}$	$0.66^{0.06}_{0.07}$	257^{127}_{133}	307^{165}_{143}	$3.0^{3.2}_{2.9}$	0.7
V1228 Ori	$3.04^{0.80}_{1.54}$	$9.18^{0.78}_{0.65}$	$37.33^{5.33}_{2.67}$	$0.48^{0.17}_{0.10}$	$0.62^{0.05}_{0.08}$	135^{74}_{74}	359^{50}_{354}	$1.7^{1.8}_{1.6}$	0.4
V1501 Ori	$3.41^{0.82}_{0.69}$	$12.19^{0.99}_{1.29}$	$42.42^{4.09}_{5.42}$	$0.59^{0.18}_{0.15}$	$0.79^{0.11}_{0.07}$	301^{105}_{97}	384^{180}_{307}	$2.5^{2.7}_{2.4}$	0.6
V1496 Ori	$3.27^{0.83}_{0.84}$	$13.00^{2.11}_{1.44}$	$65.90^{18.16}_{10.35}$	$0.27^{0.09}_{0.07}$	$0.41^{0.05}_{0.05}$	210^{556}_{186}	36^{286}_{31}	$1.6^{1.7}_{1.6}$	0.4
2MASS1	$14.49^{0.82}_{0.82}$	$12.07^{1.61}_{1.32}$	$47.93^{9.85}_{6.32}$	$1.27^{0.27}_{0.28}$	$1.08^{0.18}_{0.18}$	–	770^{246}_{293}	$3.6^{3.8}_{3.4}$	0.9
COUP 450	$30.95^{0.78}_{0.78}$	–	$34.92^{1.55}_{1.34}$	–	$5.58^{0.12}_{0.26}$	–	460^{603}_{302}	$11.2^{0.5}_{0.6}$	3.3
Par 1936	$16.88^{1.94}_{1.76}$	$13.28^{1.54}_{1.42}$	$83.00^{7.00}_{7.05}$	$0.80^{0.21}_{0.16}$	$0.26^{0.03}_{0.02}$	–	356^{1089}_{356}	$1.3^{1.4}_{1.2}$	0.3
COUP 662	$21.52^{1.66}_{1.60}$	–	$89.00^{1.00}_{1.00}$	$0.00^{0.00}_{0.00}$	$0.62^{0.02}_{0.02}$	–	364^{729}_{359}	$2.6^{2.7}_{2.5}$	0.6
V1398 Ori	$5.01^{1.05}_{1.24}$	$12.89^{1.31}_{1.00}$	$79.00^{11.00}_{11.05}$	$0.50^{0.12}_{0.16}$	$0.36^{0.06}_{0.02}$	197^{121}_{195}	415^{314}_{290}	$1.7^{1.7}_{1.6}$	0.4

Note—(1) 10^{21} cm^{-2} (2) 10^6 K (3) 10^{54} cm^{-3} (4) km s^{-1} (5) 10^{-13} erg cm^{-2} s^{-1} (6) 10^{31} erg s^{-1}

only for cases with no pileup in the spectrum. A two-temperature APED model was used for the continuum in each case and the emission lines were fit with Gaussian profiles. The ratio was used to interpolate the N_H transmission curves. The Ne-based N_H values are consistent with t the ones from the APED fits.

4.4.3. *Coronal Temperatures*

Table 6 shows all the APED temperatures of the spectral fits. Most spectra responded to the two APED components with only moderate absorption. About half a dozen sources are so absorbed that we only detect one hot component. The sources with low or moderate temperatures produced a moderately hot APED component of 6 to 19 MK. The temperatures of APED components are determined by the observed relative line strengths within an ion species and the strength of the underlying continuum. The uncertainties of this temperature component are relatively small indicating it is well determined specifically due a high number of contributing

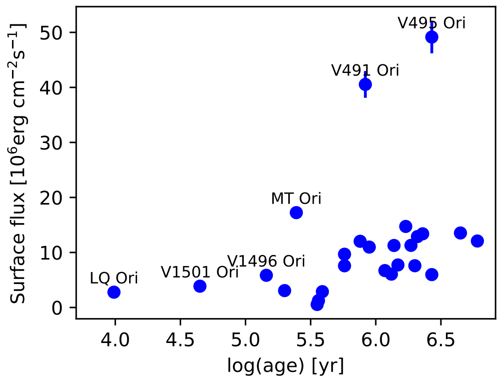

Figure 9. The surface flux plotted against the modeled age of the ONC stars The ages are taken from the COUP tables, the surface flux is the source luminosity divided by the stellar surface area. The latter was determined from the bolometric luminosity and the effective surface temperature, both also from the COUP tables. An interactive version of this figure is available in the online journal with the ability to zoom, pan, and display name and additional information for each source. The data behind the Figure (DbF) is available in the electronic table, which combines the information from Table 4 and 6.

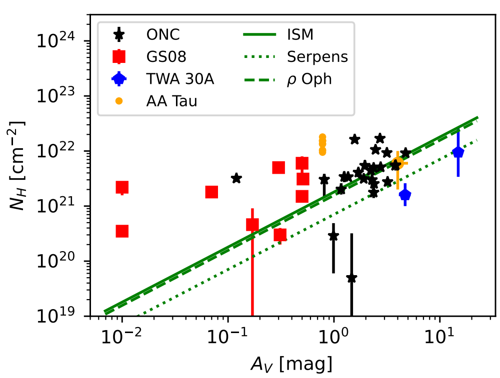

Figure 10. The N_H from the APED fits plotted versus the N_H determined from optical extinction A_V in comparison to AA Tau (the small dots without error bars are measurements before the dimming) and TWA 30A. Red squares are from the the sample from Günther & Schmitt (2008, GS08). Green lines show the N_H/A_V ratio observed in the ISM and the average value for two other star forming regions. Data sources are given in section 4.4.2. Only for AA Tau and TWA 30A extinction and absorption data are contemporaneous, while all other cases rely on optical and X-ray data taken non-contemporaneously. An interactive version of this figure is available in the online journal with the ability to zoom, pan, and display name and additional information for each source. Clicking on the legend entries mutes/unmutes the data for better visibility. The data behind the Figure (DbF) is available in the electronic table, which combines the information from Table 4 and 6.

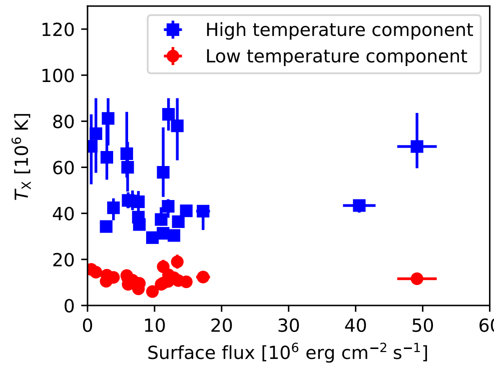

Figure 11. The coronal temperatures from the APED fits versus the surface flux. An interactive version of this figure is available in the online journal with the ability to zoom, pan, and display name and additional information for each source. The data behind the Figure (DbF) is available in the electronic table, which combines the information from Table 4 and 6.

lines. In that respect the spread in temperature between the ONC stars is likely real.

Figure 11 plots all temperatures against surface flux. The very hot component not only shows quite a large scatter between 30 MK and 90 MK, but likely a bifurcation of values. It shows the presence of two temperature regimes, one between 30 and 50 MK, and a very hot one between 60 MK and 90 MK. While in the case of the hot components there are a few supporting lines from Si, S, Ar and Ca, the very hot component at best has line contributions from Fe XXV and Fe XXVI but is mostly defined by the continuum. Of the highly absorbed stars there is only one, COUP 662, that exhibited an extremely high temperature component at 89 MK, which has no lines associated with the detected continuum. Another interesting case is V495 Ori, which is bright in only two observations and exhibits a giant flare. Its shows a moderate and a very hot component of 69 MK indicating that sources with very hot components likely engage in heavy flaring.

It is also important to consider the underlying emission measure contributions. For the two components we measure values between a few times 10^{53} cm^{-3} and 10^{54} cm^{-3}. This shows that the ensemble of coronal stars exhibit fairly consistent properties. These are, except for MT Ori, slightly smaller than the ones determined in the early observations (Schulz et al. 2015), but not by much. However, there are some significant trends with respect to X-ray temperature. The first is that on average the emission measures of the low temperature component ($\sim$ 10 MK) is about a factor 2-3 smaller than that of the hot component ($\sim$ 40 MK). This is not the case for the very hot component (> 60 MK) which is similar or

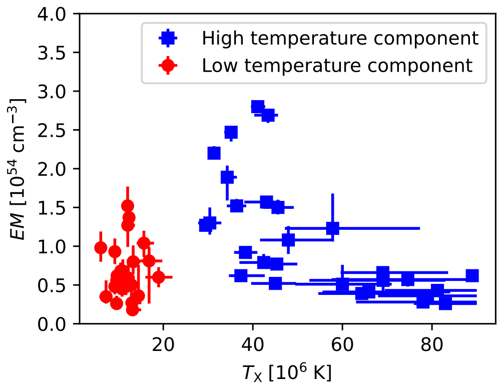

Figure 12. The emission measures from the APED fits plotted versus the temperatures from the fits. This figure is zoomed in to avoid large values in MT Ori and V450 Ori. An interactive version of this figure is available in the online journal with the ability to zoom, pan, and display name and additional information for each source. The data behind the Figure (DbF) is available in the electronic table, which combines the information from Table 4 and 6.

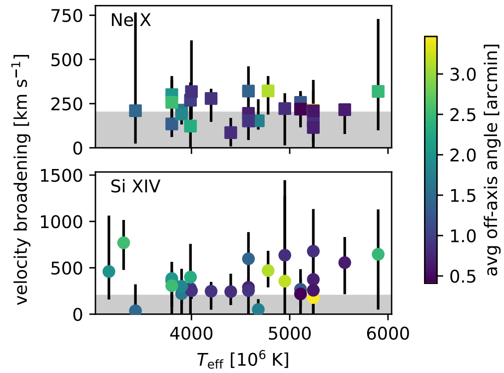

Figure 13. The measured line widths from the single line fits. The symbol color indicates how far off axis the source is located, averaged over all observations. An interactive version of this figure is available in the online journal with the ability to zoom, pan, and display name and additional information for each source. Clicking on the legend entries mutes/unmutes the data for better visibility. The data behind the Figure (DbF) is available in the electronic table, which combines the information from Table 4 and 6.

even lower in value than the one associated with the low temperature component. Thus it appears that all three X-ray temperature regimes possess distinct properties with respect to their coronal nature with respect to emission volume and maybe even plasma densities.

One item we did not pursue in this global coronal analysis is a more detailed study of abundances, which should be done in more detailed followup studies of this coronal sample. However we did perform a pre-fit of APED abundance values, which can be useful already. However, when we determine a set of average values we need to optimize the sample. For example, for highly absorbed sources values for Ne and Mg are more unreliable because only a few weak lines might exist. Similarly we might exclude high Z element abundances from the subset of very high temperature components because lines are weak and/or likely only some Fe K lines exist. In calculating the average values for the remaining sources we also drop the highest and lowest values to remove some bias where the fit was unable to make a sensible determination. The average abundance distribution for the coronal fits then yields the following values with respect to solar (Anders & Grevesse (1989)): Ne (1.52+/-0.70), Mg (0.18+/-0.16), Si (0.20+/-0.13), S (0.28+/-0.21), Ar (0.59+/-0.45), Ca (0.26+/-0.25), Fe (0.14+/-0.18). The +/- values are not uncertainties but the variance from the avarage in the sample.

4.4.4. *Line Dynamics*

The broadband fits were conducted with unbroadend line contributions, i.e. APED lines were treated as delta functions with no thermal and turbulent contributions. This was quite warranted as the continua were dominating the fit and thermal and turbulent contributions are expected to be relatively small in coronal sources. It also guarantees that specifically in the hotter components, where lines are weak and absent, line widths do not run away during the fits as dilute the continuum fit.

However, in order to test that assumption we also performed separate line fits to the bright lines in the spectrum. The best cases were the Ne X and the Si XIV lines, both H-like single line systems. We ignored the spin-orbit coupling and fitted these lines with single Gaussian line functions at the appropriate wavelength. Here we also have to worry about the spatial distribution of sources. The stars in Tab. 4 distribute around the aim-point within about 3 arcmin radius. The HETG instrument can tolerate zeroth orders to about 2 arcmin off-axis and not suffer degradation of spectral resolution. This means that about 25% of the stars in Tab. 4 will suffer some form of spectral degradation. We plotted all line fits in Fig. 13 and color coded the off-axis information.

To further quantify line broadening, since we do not expect it in typical coronal sources, we took one case to investigate in more detail. MT Ori has well detected broadening in Ne X. We started with the two-temperature plasma model (see Table 6) and allowed the turbulent broadening term and the redshift to be free parameters and re-fit the merged spectrum over the 8–14 Å region where there are many lines from Mg, Ne, and Fe. We also let the normalization float (but tied the ratio), but kept the two temperatures frozen. In addi-

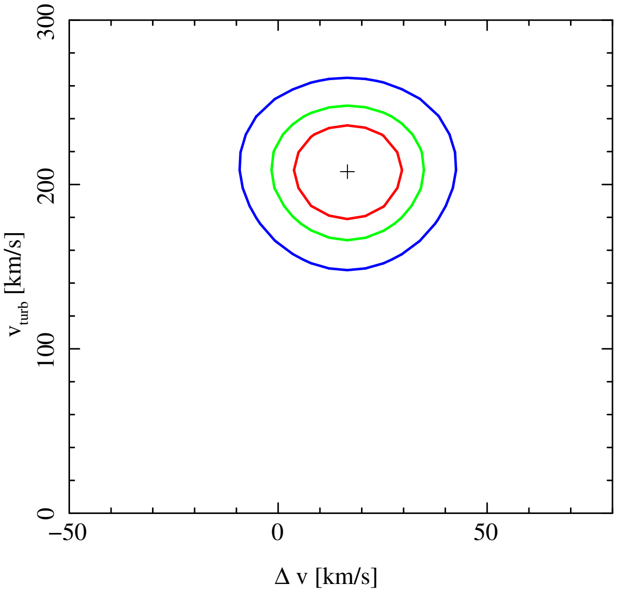

Figure 14. The confidence contours for the turbulent broadening term against Doppler shift for a plasma model fit to the 8–14 Å region of MT Ori. Contours are for 68%, 90%, and 99% limits.

tion, we allowed relative abundances of Mg, Ne, and Fe to be free. In this way, we implicitly include all blending implicit in the model, account for thermal broadening, and determine any excess broadening required to fit the spectrum. This confirms the result found for fitting individual features. We show the confidence contours of the excess broadening against the Doppler shift in Figure 14, and contours are closed. This is a barely resolved result — if the broadening were a bit lower ($v_{\rm turb} \gtrsim 100\,{\rm km\,s^{-1}}$), then the contours would likely be unbounded on the lower limit. We suspect that broadening in this case could be due to orbital motions in a binary system.

4.4.5. θ^1 *Ori E*

θ^1 Ori E is a spectroscopic binary with a 9.9 day period in which both components, each a G-type giant, have an intermediate mass of about $2.8\,M_\odot$. The basic characteristics were reviewed by Huenemoerder et al. (2009), along with a detailed analysis of the HETG spectrum. We now have an effective exposure of about 1.5 Ms, compared to the previous 260 ks. Due to detector efficiency reduction and source confusion, the largest exposure gains are in the short wavelength region, below 10 Å and we fully realize the expected increase in signal-to-noise ratio of 2 or more. This will allow us to put better constraints on the highest temperature plasma through the continuum emission and the emission from the H- and He-like ions of Si, S, Ar, Ca, and Fe. Here we provide an overview of the improved spectrum, with a look at an approximate plasma model, variability, and line profiles.

A three-temperature APED model provided an overall characterization of this high brilliance spectrum, but as we noticed for θ^1 Ori C, there were large residuals that could not be eliminated with few-temperature-component models. We thus adopted a broken power-law emission measure distribution model which approximates the line-based emission-measure reconstruction of Huenemoerder et al. (2009). The model parameters are the normalization, the temperature of maximum emission measure, and powerlaw slopes below and above that temperature, and relative elemental abundances; fitted values are given in Table 7. Uncertainties for the emission measure shape were determined from a Monte-Carlo evaluation, with relative abundances frozen. The Fe and Ni values were determined post-facto from confidence levels determined using only the 10–13 Å region, which has many Fe lines and the brightest Ni lines. The oxygen abundance uncertainty was scaled from the flux uncertainty, and is the most uncertain value due to the low counts in that region, due both to line-of-sight absorption and detector contamination. Portions of the spectra and models are shown in Figure 15 and 16.

The plasma model fits include a "turbulent" velocity term and a redshift. Emission lines were also fit individually with Gaussian profiles. The lines in the merged spectrum showed significant excess broadening (in addition to instrumental or thermal terms), having about $400\,{\rm km\,s^{-1}}$ full-width-half-maximum with an uncertainty of $50\,{\rm km\,s^{-1}}$ (corresponding to $v_{\rm turb} \approx 200 \pm 30\,{\rm km\,s^{-1}}$). The maximum orbital radial velocity separation is about $160\,{\rm km\,s^{-1}}$. Since the spectrum fit was merged over all observations, we expect there to be some width due to orbital dynamics. However, the measured width is somewhat larger than expected from photospheric radial velocities alone. The mean profile Doppler shifts are consistent with $0.0 \pm 30\,{\rm km\,s^{-1}}$ (not accounting for heliocentric motion). The values are consistent with Huenemoerder et al. (2009), but have smaller uncertainties. The widths and offsets definitely need further scrutiny, especially relative to orbital phase.

With this deeper exposure of θ^1 Ori E we have significantly improved diagnostics from the 2–7 Å region, specifically from the emission lines of Si, S, Ar, and Ca. The broken powerlaw emission measure model, though, may be too simple, since the model seems to under-predict Fe XXV, as seen in the residuals in Figure 15.

θ^1 Ori E is highly variable. As a broad overview of this, we fit the mean flux in a hard band (1.7–7.0 Å) and in a soft band (7.0–20.0 Å) and formed a hardness-

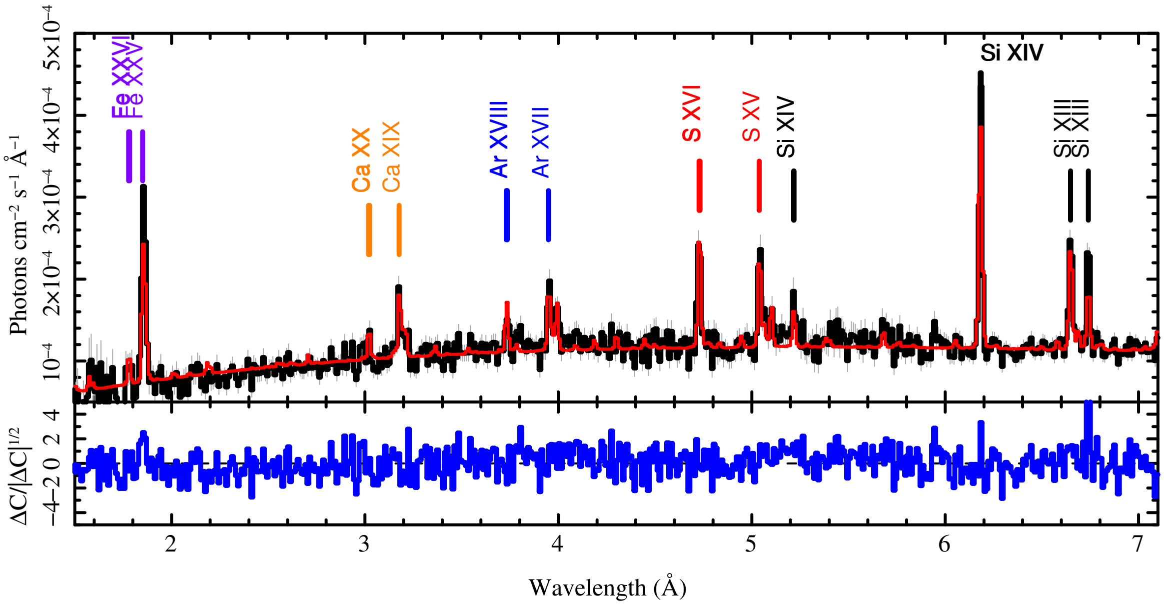

Figure 15. The short-wavelength region HETGS spectrum of θ^1 Ori E, having an effective exposure of 1.5 Ms. The prominent H- and He-like emission lines are labeled. The flux spectrum is shown in black, the model in red, and residuals in the lower panel. Line label colors are arbitrary.

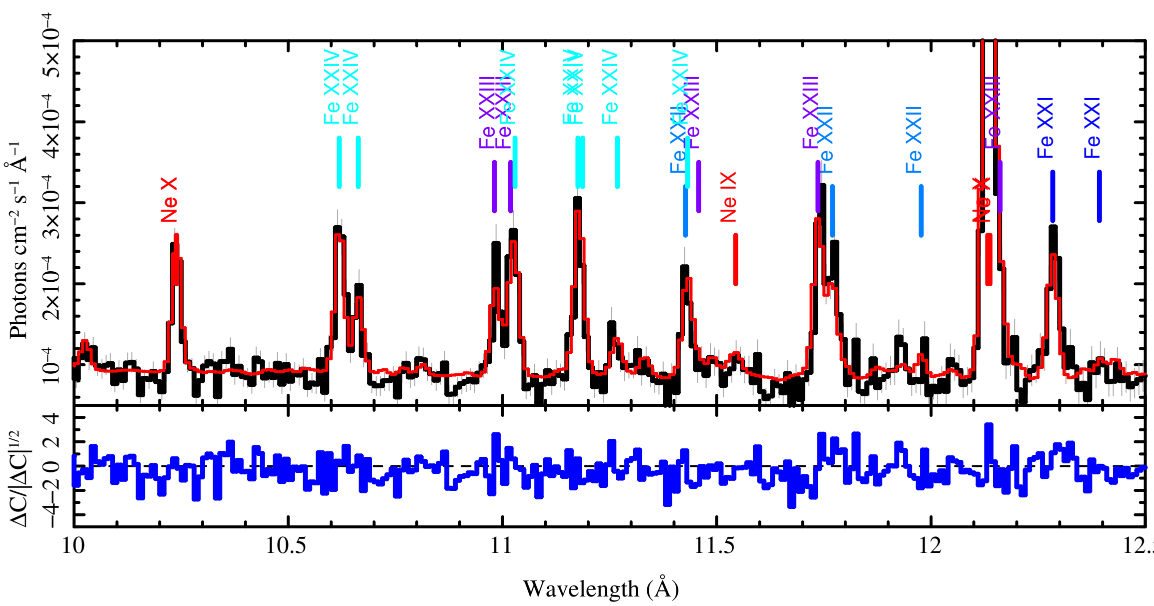

Figure 16. The 10–13 Å region HETGS spectrum of θ^1 Ori E, which is important for establishing the relative Fe and Ni abundances, given the emission measure model. The fluxed spectrum is shown in black, the model in red, and below are the residuals. Prominent emission from Fe XXI to Fe XXIV are labeled, as well as some neon lines (label colors are arbitrary).

ratio, $HR = (H - S)/(H + S)$, where H and S refer the the hard and soft band fluxes. in Figure 17 we plot the HR against H for each individual *Chandra* observation. This shows over an order of magnitude range in H, in a direct correlation with HR. The flux-hardness trend, is likely due to coronal magnetic flare events. This is consistent with one of the defining characteristics of stellar coronal (magnetic) flares, that they are hotter and brighter.

The abundance of Ne seems significantly larger than determined by Huenemoerder et al. (2009), either due to flaring, or could be due to emission measure distribution structure, which will require more careful evaluation using reconstruction using line fluxes, or via exploration of more complex emission measure models. Abundances of

Table 7. Broken Powerlaw Emission Measure Model Parameters

Parameter	Value
Norm	6.3×10^{-3} (1.0×10^{-4}) [cm^{-5}]
$T_{\max}$	26.3 (2.4) MK
α	0.9 (0.1)
β	−2.5 (0.2)
O	0.22 (0.08)
Ne	0.82 (0.08 :)
Mg	0.30 (0.03 :)
Si	0.22 (0.02 :)
S	0.25 (0.04 :)
Ar	0.58 (0.1 :)
Ca	0.84 (0.2 :)
Fe	0.17 (0.01)
Ni	0.11 (0.06)

Note—Model parameters, for an emission model defined by $EM(T) = Norm * (T/T_{\max})^{a(T)}$; $a(T < T_{\max}) = \alpha$; $a(T \geq T_{\max}) = \beta$. Elemental abundances are given relative by number to the fiducial values of Anders & Grevesse (1989). The emission measure and normalization are related in the usual scaling: $EM = 10^{14} \times Norm/(4\pi d^2)$ [cm^{-3}]. Abundance uncertainties not formally evaluated, but estimated from counts are designated with a ":".

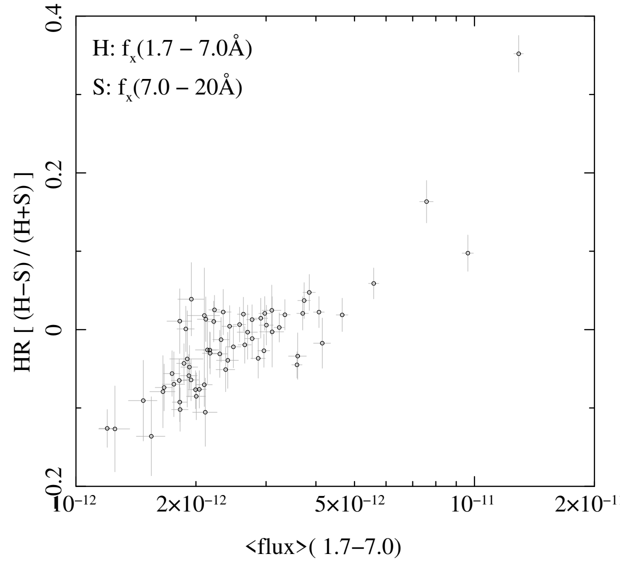

Figure 17. The hardness ratio vs. hard flux for θ^1 Ori E. Each point represents a single observation ID. A hardness increasing directly with flux is a characteristic of stellar coronal flares (magnetic reconnection events).

Ca, Ar, and Ni are consistent with upper limits of previously determined values, but now much better constrained.

5. SUMMARY AND OUTLOOK

This data set was designed to provide the first collection of high resolution X-ray spectra of a very young massive stellar cluster. We were able to harvest about three dozen of high resolution X-ray spectra from young massive, intermediate mass, and low mass stars with sufficient statistical properties to determine spectral fluxes, coronal temperatures, line widths, line ratios, and abundances. This data set now provides a unique base of high resolution X-ray spectra of some of the youngest stars known. The ONC cluster study provides common initial conditions for all extracted objects: stars are chemically similar, they have young ages, a common ISM evolution and are exposed to fairly similar global extinction. To be clear this first extraction is not designed to provide detailed physical results of the involved extracted stars but an overall characterization of the X-ray spectra and global properties.

The sample of extracted HETG spectra includes four massive stars. The most prominent star is θ^1 Ori C (Schulz et al. 2000, 2003; Gagné et al. 2005) with over 10^6 of total counts in 1st order providing for high S/N at the provided oversampling of each HETG resolution element which will allow for high brilliance line profile studies and weak line searches (see Gagne et al. 2024, in prep.). One most intriguing outcome of the long exposure for this star is the potential use of higher order grating data, which in this case resolves high Z He-like triplets of Mg, Si, S, Ar Ca, and Fe with unprecedented high resolution. Plasma density and UV pumping studies should be highly beneficial for future high resolution missions. θ^2 Ori C is the second most massive star in the sample and here the survey added only about 10^4 counts to the previously existing data as published in (Schulz et al. 2006; Mitschang et al. 2011). The new data should primarily improve the the study of Mg and Si lines. The zero order data shows high variability in the source indicating that the star system did engage in flaring activity as reported in Schulz et al. (2006) and while the HETG 1st order covers only a fraction of this activity it should prove essential in the in depth flare analysis. Another interesting but also unfortunate outcome of the survey is the almost complete absence of θ^1 Ori D in HETG 1st order and also a surprising weakness in 0th order. The latter is likely a result of the fact that softer X-rays are blocked by detector contamination. More interesting is the collection of over $7{\times}10^4$ counts in θ^1 Ori A, a massive trapezium star that is in type an companion count very similar to θ^1 Ori D, a fact that certainly needs further study. The fifth massive star in the sample is V1230 Ori, which is not part of the Orion Trapezium and farther away in the ONC. Since the survey could not produce any 1st order spectra for θ^1 Ori B and θ^2 Ori B, the 2.4×10^4 counts in HETG 1st order are the only data to study later B-type massive stars.

The survey also produced over 30 HETG 1st order spectra of intermediate mass and low-mass CTTS which at their current evolutionary state should exhibit accretion and coronal signatures. At a canonical age of the ONC of around 1 Myr and older we expect mostly the latter. The θ^1 Ori E binary and MV Ori are the most massive stars in our sample. The deeper exposure of θ^1 Ori E improves the determination of the high-temperature emission measure and elemental abundances through the well-detected emission lines of Si, S, Ar, Ca, and Fe in the 1.8–7 Å spectral region. The longer exposure also better quantifies the variability as typical of coronal flares. Future work is needed to improve the emission measure distribution, since it probably has more structure than our adopted provisional model, to study the distribution at different emission levels to help model flaring structures, and to phase resolve line-shifts and broadening to further model the emission from each stellar binary component.

We analyzed all the other stars with a two temperature coronal plasma model to characterize their global coronal properties. From these fits we determined X-ray fluxes between 1.3×10^{-13} erg cm^{-2} s^{-1} and 3.4×10^{-12} erg cm^{-2} s^{-1} with the bulk of the fluxes trending more to the low end of these limits. Most ONC stars are even fainter. The extraction procedure in Sect. 2 shows that more exposure would not result in more sources with successfully extracted first order spectra but only more dominating source confusion resulting in loss of exposure. In that respect this survey is going to the limit of what the high resolution gratings can achieve in a crowded cluster field.

From the extracted sample we can see that if we describe X-ray activity in terms of surface flux, then Fig. 9 might show that activity increases with age in CTTS, even though not as strongly as was suggested in Schulz et al. (2015). The surface fluxes of the bulk of the ONC stars appear quite similar to other CTTS stars. What is striking in these global fits is the distribution of coronal temperatures. A large number of ONC stars can be described by a bi-modal temperature distribution, where one temperature is around 10 MK, the other one more around 40 MK. This is what Schulz et al. (2015) observed in the six bright ONC CTTS and is no surprise. It is observed in many other CTTS outside the ONC, such as TW Hya (Kastner et al. 2002), HD 9880 (Kastner et al. 2004), and BP Tau (Robrade & Schmitt 2006) to mention a few of the many we know today. Here we see these common properties in almost three dozen T Tauri stars of a single cluster. What is new is that there is a subsample of sources where the high temperature component is more like 60 MK and higher, something that is not expected under normal coronal conditions. This definitely requires further study. It is interesting to note that the emission measures of the two normal temperature components distribute somewhat similar to what was projected in Schulz et al. (2015) but not as extreme, the average between high and low temperatures differ more like 2.5 instead of the factor 3 to 6. However, it should be noted that in the cases of the very high temperatures, the emission measures are systematically low indicating that here we may deal with high plasma densities and low volumes.

CTTS are also characterized by active accretion and in some nearby stars with low absorption, accretion signatures are seen prominently in the grating spectra: The line ratios in the He-like triplets of O VII and Ne IX have unusually low forbidden to intercombination (f/i) line ratios, that can only be explained by high densities in the emission region (Kastner et al. 2002; Brickhouse et al. 2010). The observed densities are higher than seen in the corona and do not correlate with flares, thus a natural explanation is for the emission to come from the cooling flow behind the accretion shock. Unfortunately, the data presented here cannot be used to test for this as the high contamination on the ACIS camera makes those lines inaccessible to us. The other signature of accretion seems to be an excess of soft plasma when comparing accreting and non-accreting CTTS (Robrade & Schmitt 2007; Telleschi et al. 2007), which could again be a direct signature of the post-shock cooling flow or an indirect effect where the presence of accretion columns cools or distorts the fields in the corona (Schneider et al. 2018). Again, the low sensitivity of ACIS in our observations and the high absorbing column densities for many objects in the ONC make it hard to test for this conclusively. Based on our knowledge of CTTS in other star forming regions, it seems very likely that accretion does contribute to the soft X-ray emission in our target stars and thus influences their disk evolution, even though this is not directly observable in our dataset.

The X-ray absorbing column density and the optical/IR extinction (or "reddening") probe different aspects of the material in the line-of-sight. The optical extinction is typically expressed as dimming in a certain band, e.g. A_V, and it is caused by small dust grains. The

X-ray absorption is dominated by inner-shell absorption of heavy elements with contribution from H and He; this absorption occurs both in gas and small dust grains. Only large grains that block all energies of X-ray light do not change the shape of the observed X-ray spectrum; instead they cause grey absorption that just reduces the overall intensity. The X-ray absorbing column density is measured as $N_{\rm H}$, the equivalent hydrogen column density that would cause the observed absorption for some standard set of elemental abundances. A naive interpretation of the $N_{\rm H}/A_V$ ratio is that this measures the gas-to-dust ratio averaged over the line-of-sight. However, grain growth and non-standard abundances also influence the measured ratio and might be different in the accretion columns, the disk atmosphere, the cloud material, and the ISM between the ONC and Earth.

One promising approach is to study time variability, where the time scale can give us a hint in which region the absorber is located. Principe et al. (2016) observed a change in $N_{\rm H}$ over a month, but with constant $N_{\rm H}/A_V$ ratio, in TWA 30. This star is seen nearly edge-on, so we are looking through some layer of the disk, with different column density at different times or locations, but constant dust grain properties. In AA Tau, Grosso et al. (2007) observed repeated changes of $N_{\rm H}$ over the 8-day rotation period consistent with a wedge of the inner disk rotating in and out of view; this inner part of the disk appears gas rich, while an outer ($R > 1$ au) dimming indicates ISM like material (Schneider et al. 2015). Another prominent example is RW Aur (Günther et al. 2018) which showed an increase in $N_{\rm H}$ by a factor > 100 over time scales of months to years, clearly related to major changes in the disk structure. In our general analysis in the ONC, we do not have the time information as in these examples, but we can look at the properties of the sample. Figure 10 shows ONC sources both above and below the line of an ISM-like $N_{\rm H}/A_V$ ratio. While there are certain systematics in the measurement of both $N_{\rm H}$ and A_V, this spread is likely real and represents the different viewing geometries. If the line-of-sight passes though a structure close to the star, within the dust sublimation radius, $N_{\rm H}/A_V$ is large. For a star seen at high inclination angle, the structure could be a polar accretion column, while for stars at lower inclination, the inner disk might contribute. On the other hand, stars seen through the outer disk might have more evolved dust grains, leading to low $N_{\rm H}/A_V$ values. Since disks are dynamic, this processed dust can be lifted into higher layers of the disk and might be in the line-of-sight, even we do not view the star through the disk mid-plane.

Of the 45 stars in this study, 33 are known variables, 7 are suspected variables, 4 have not been identified as variable, and one was excluded due to pileup in the zeroth order. These statistics allow us to carry out a time-resolved analysis of a significant number of flares in a population of cool stars of approximately the same age. For several of the identified flares, high resolution spectra can be obtained starting before the flare begins to be visible in the X-rays and continue through the end of the X-ray emission of the flare. Such an analysis technique is rare in the study of flares due to their unpredictable nature. The flare spectra will be analyzed to determine spectral changes during the flares.

The percent of obsids that are probably or definitely variable for each source ranges from 0% to 36%. Of course, the longer the exposure time of an obsid, the greater the possibility of detecting variability. But the statistics for each source include the same set of obsids (except those with known zeroth order confusion) of the same exposure time, so the variability percent is relevant and should be considered in concert with the presence of flares and periodicity. Light curves produced by the glvary tool for each obsid are being evaluated to verify the timing and duration of flares detected by the statistical method

.... This project was funded by Chandra grant GO0-21015A and by NASA through the Smithsonian Astrophysical Observatory (SAO) contract SV3-73016 to MIT for Support of the Chandra X-Ray Center (CXC) and Science Instruments. CXC is operated by SAO for and on behalf of NASA under contract NAS8-03060. N.S. would like to thank MKI postdoctoral associate Jun Yang for participation and comments. J.N. acknowledges the assistance of Thomas Firnhaber (University of Kansas) in the zeroth order variability analysis. The research of T.P. was partly supported by the Deutsche Forschungsgemeinschaft (DFG, German Research Foundation) under Germany's Excellence Strategy - EXC 2094 - 390783311. T.P. would like to thank the LMU PhD students S. Flaischlen and C. Göppl for assistance in the preparation of data tables for this project. The team would also like to thank Wayne Waldron for helpful comments early in the project.

REFERENCES

Anders, E., & Grevesse, N. 1989, GeoCoA, 53, 197

Argiroffi, C., Maggio, A., & Peres, G. 2007, A&A, 465, L5

Argiroffi, C., Maggio, A., Montmerle, T., et al. 2012, ApJ, 752, 100

Bally, J., O'Dell, C. R., & McCaughrean, M. J. 2000, AJ, 119, 2919

Brickhouse, N. S., Cranmer, S. R., Dupree, A. K., Luna, G. J. M., & Wolk, S. 2010, ApJ, 710, 1835

Broos, P. S., Feigelson, E. D., Townsley, L. K., et al. 2007, ApJS, 169, 353

Broos, P. S., Townsley, L. K., Feigelson, E. D., et al. 2011, ApJS, 194, 2

Canizares, C. R., Huenemoerder, D. P., Davis, D. S., et al. 2000, ApJL, 539, L41

Crowther, P. A., Broos, P. S., Townsley, L. K., et al. 2022, MNRAS, 515, 4130

Da Rio, N., Robberto, M., Soderblom, D. R., et al. 2010, ApJ, 722, 1092

den Boggende, A. J. F., Mewe, R., Gronenschild, E. H. B. M., Heise, J., & Grindlay, J. E. 1978, A&A, 62, 1

Espaillat, C. C., Robinson, C. E., Romanova, M. M., et al. 2021, Nature, 597, 41

Fabricius, C., Luri, X., Arenou, F., et al. 2021, A&A, 649, A5

Feigelson, E. D., & Decampli, W. M. 1981, ApJL, 243, L89

Feigelson, E. D., Getman, K., Townsley, L., et al. 2005, ApJS, 160, 379

Feigelson, E. D., Getman, K. V., Townsley, L. K., et al. 2011, ApJS, 194, 9

Fruscione, A., McDowell, J. C., Allen, G. E., et al. 2006, in Presented at the Society of Photo-Optical Instrumentation Engineers (SPIE) Conference, Vol. 6270, SPIE Conference Series

Gagne, M., Caillault, J.-P., & Stauffer, J. R. 1995, ApJ, 445, 280

Gagné, M., Oksala, M. E., Cohen, D. H., et al. 2005, ApJ, 628, 986

Gagné, M., Fehon, G., Savoy, M. R., et al. 2011, ApJS, 194, 5

Getman, K. V., Flaccomio, E., Broos, P. S., et al. 2005, ApJS, 160, 319

Giacconi, R., Murray, S., Gursky, H., et al. 1972, ApJ, 178, 281

GRAVITY Collaboration, Karl, M., Pfuhl, O., et al. 2018, A&A, 620, A116

Gregory, P. C., & Loredo, T. J. 1992, ApJ, 398, 146

Grellmann, R., Preibisch, T., Ratzka, T., et al. 2013, A&A, 550, A82

Grosso, N., Bouvier, J., Montmerle, T., et al. 2007, A&A, 475, 607

Güdel, M., Audard, M., Bacciotti, F., et al. 2011, in Astronomical Society of the Pacific Conference Series, Vol. 448, 16th Cambridge Workshop on Cool Stars, Stellar Systems, and the Sun, ed. C. Johns-Krull, M. K. Browning, & A. A. West, 617

Günther, H. M., Liefke, C., Schmitt, J. H. M. M., Robrade, J., & Ness, J.-U. 2006, A&A, 459, L29
Günther, H. M., & Schmitt, J. H. M. M. 2008, A&A, 481, 735
Günther, H. M., Schmitt, J. H. M. M., Robrade, J., & Liefke, C. 2007, A&A, 466, 1111
Günther, H. M., Birnstiel, T., Huenemoerder, D. P., et al. 2018, AJ, 156, 56
Hartmann, L., Herczeg, G., & Calvet, N. 2016, ARA&A, 54, 135
Herbig, G. H., & Griffin, R. F. 2006, AJ, 132, 1763
Hillenbrand, L. A. 1997, AJ, 113, 1733
Hillenbrand, L. A., Hoffer, A. S., & Herczeg, G. J. 2013, AJ, 146, 85
Houck, J. C., & Denicola, L. A. 2000, in Astronomical Society of the Pacific Conference Series, Vol. 216, Astronomical Data Analysis Software and Systems IX, ed. N. Manset, C. Veillet, & D. Crabtree, 591
Huenemoerder, D. P., Kastner, J. H., Testa, P., Schulz, N. S., & Weintraub, D. A. 2007, ApJ, 671, 592
Huenemoerder, D. P., Schulz, N. S., Testa, P., Kesich, A., & Canizares, C. R. 2009, ApJ, 707, 942
Karl, M., Pfuhl, O., Eisenhauer, F., Genzel, R., & Grellmann, R. e. a. 2018, A&A, 620, A116
Kastner, J. H., Franz, G., Grosso, N., et al. 2005, ApJS, 160, 511
Kastner, J. H., Huenemoerder, D. P., Schulz, N. S., et al. 2004, ApJL, 605, L49
Kastner, J. H., Huenemoerder, D. P., Schulz, N. S., Canizares, C. R., & Weintraub, D. A. 2002, ApJ, 567, 434
Kastner, J. H., Zuckerman, B., Weintraub, D. A., & Forveille, T. 1997, Science, 277, 67
Kounkel, M., Hartmann, L., Loinard, L., et al. 2017, ApJ, 834, 142
Kraus, S., Weigelt, G., Balega, Y. Y., et al. 2009, A&A, 497, 195
Kuhn, M. A., Hillenbrand, L. A., Sills, A., Feigelson, E. D., & Getman, K. V. 2019, ApJ, 870, 32
Lamzin, S. A. 1998, Astronomy Reports, 42, 322
Lindegren, L. 2018, gAIA-C3-TN-LU-LL-124
Lindegren, L., Bastian, U., Biermann, M., et al. 2021, A&A, 649, A4
Maíz Apellániz, J., Barbá, R. H., Fernández Aranda, R., et al. 2022, A&A, 657, A131
Manara, C. F., Robberto, M., Da Rio, N., et al. 2012, ApJ, 755, 154
Menten, K. M., Reid, M. J., Forbrich, J., & Brunthaler, A. 2007, A&A, 474, 515
Mitschang, A. W., Schulz, N. S., Huenemoerder, D. P., Nichols, J. S., & Testa, P. 2011, ApJ, 734, 14
Muench, A. A., Lada, E. A., Lada, C. J., & Alves, J. 2002, ApJ, 573, 366
Olivares, J., Sarro, L. M., Bouy, H., et al. 2020, A&A, 644, A7
Orlando, S., Sacco, G. G., Argiroffi, C., et al. 2010, A&A, 510, A71
Orlando, S., Bonito, R., Argiroffi, C., et al. 2013, A&A, 559, A127
Petr, M. G., Coudé du Foresto, V., Beckwith, S. V. W., Richichi, A., & McCaughrean, M. J. 1998, ApJ, 500, 825
Pillitteri, I., Wolk, S. J., Megeath, S. T., et al. 2013, ApJ, 768, 99
Preibisch, T., Balega, Y., Hofmann, K.-H., Weigelt, G., & Zinnecker, H. 1999, NewA, 4, 531
Preibisch, T., Hodgkin, S., Irwin, M., et al. 2011, ApJS, 194, 10
Principe, D. A., Sacco, G., Kastner, J. H., Stelzer, B., & Alcalá, J. M. 2016, MNRAS, 459, 2097
Reale, F., Orlando, S., Testa, P., Landi, E., & Schrijver, C. J. 2014, ApJL, 797, L5
Reale, F., Orlando, S., Testa, P., et al. 2013, Science, 341, 251
Robberto, M., Soderblom, D. R., Scandariato, G., et al. 2010, AJ, 139, 950
Robrade, J., & Schmitt, J. H. M. M. 2006, A&A, 449, 737
—. 2007, A&A, 473, 229
Rots, A. H. 2012, in New Horizons in Time Domain Astronomy, ed. E. Griffin, R. Hanisch, & R. Seaman, Vol. 285, 402–403
Rzaev, A. K., Shimansky, V. V., & Kolbin, A. I. 2021, MNRAS, 504, 3787
Sacco, G. G., Orlando, S., Argiroffi, C., et al. 2010, A&A, 522, A55
Schmitt, J. H. M. M., Robrade, J., Ness, J.-U., Favata, F., & Stelzer, B. 2005, A&A, 432, L35
Schneider, P. C., France, K., Günther, H. M., et al. 2015, A&A, 584, A51
Schneider, P. C., Günther, H. M., Robrade, J., Schmitt, J. H. M. M., & Güdel, M. 2018, A&A, 618, A55
Schneider, P. C., Günther, H. M., & Ustamujic, S. 2022, arXiv e-prints, arXiv:2207.06886
Schulz, N. S., Canizares, C., Huenemoerder, D., & Tibbets, K. 2003, ApJ, 595, 365
Schulz, N. S., Canizares, C. R., Huenemoerder, D., & Lee, J. C. 2000, ApJL, 545, L135
Schulz, N. S., Huenemoerder, D. P., Günther, M., Testa, P., & Canizares, C. R. 2015, ApJ, 810, 55
Schulz, N. S., Testa, P., Huenemoerder, D. P., Ishibashi, K., & Canizares, C. R. 2006, ApJ, 653, 636

Skrutskie, M. F., Cutri, R. M., Stiening, R., et al. 2006, AJ, 131, 1163

Telleschi, A., Güdel, M., Briggs, K. R., Audard, M., & Palla, F. 2007, A&A, 468, 425

Testa, P., Drake, J. J., & Peres, G. 2004, ApJ, 617, 508

Townsley, L. K., Broos, P. S., Feigelson, E. D., et al. 2006, AJ, 131, 2140

Townsley, L. K., Broos, P. S., Corcoran, M. F., et al. 2011, ApJS, 194, 1

Vilhu, O. 1984, A&A, 133, 117

Vilhu, O., & Walter, F. M. 1987, ApJ, 321, 958

Vuong, M. H., Montmerle, T., Grosso, N., et al. 2003, A&A, 408, 581

Waldron, W. L., Cassinelli, J. P., Miller, N. A., MacFarlane, J. J., & Reiter, J. C. 2004, ApJ, 616, 542

Wang, J., Townsley, L. K., Feigelson, E. D., et al. 2008, ApJ, 675, 464

—. 2007, ApJS, 168, 100

Wolk, S. J., Spitzbart, B. D., Bourke, T. L., & Alves, J. 2006, AJ, 132, 1100

Wright, N. J., Drake, J. J., Mamajek, E. E., & Henry, G. W. 2011, ApJ, 743, 48